

可压缩Navier–Stokes方程的时空耦合优化低维动力系统建模方法

齐进, 吴锤结

Construction of Spatiotemporal-Coupling Optimal Low-Dimensional Dynamical Systems for Compressible Navier-Stokes Equations

QI Jin and WU Chuijie

在线阅读 View online: <https://doi.org/10.21656/1000-0887.430220>

您可能感兴趣的其他文章

Articles you may be interested in

不可压缩Navier–Stokes方程最优动力系统建模和分析

Analysis and Modelling of Optimal Dynamical Systems of Incompressible NavierStokes Equations

应用数学和力学. 2020, 41(1): 1–15 <https://doi.org/10.21656/1000-0887.400279>

含压力基Navier–Stokes方程最优动力系统建模和分析

Modelling and Analysis of Optimal Dynamical Systems of Incompressible Navier–Stokes Equations With Pressure Base Functions

应用数学和力学. 2020, 41(8): 817–833 <https://doi.org/10.21656/1000-0887.400276>

Navier–Stokes方程的脉动速度方程的最优动力系统建模和动力学分析

Modelling and Dynamics Analysis of Optimal Dynamical Systems of Fluctuation Velocity Equations for Incompressible Navier–Stokes Equations

应用数学和力学. 2020, 41(3): 235–249 <https://doi.org/10.21656/1000-0887.400277>

超音速探测器–刚性盘–缝–带型降落伞系统的大涡模拟研究

Large–Eddy Simulation of Supersonic Capsule–Rigid Disk–Gap–Band Parachute Systems

应用数学和力学. 2021, 42(3): 233–247 <https://doi.org/10.21656/1000-0887.410274>

不可压缩黏性流体的二维Navier–Stokes方程的间断有限元模拟

A Discontinuous Galerkin FEM for 2D Navier–Stokes Equations of Incompressible Viscous Fluids

应用数学和力学. 2020, 41(8): 844–852 <https://doi.org/10.21656/1000-0887.400379>

基于Picard迭代的 $P_N \times P_{N-2}$ 谱元法求解定常不可压缩Navier–Stokes方程

A $P_N \times P_{N-2}$ Spectral Element Method Based on the Picard Iteration for Steady Incompressible Navier–Stokes Equations

应用数学和力学. 2021, 42(2): 142–150 <https://doi.org/10.21656/1000-0887.410289>



关注微信公众号，获得更多资讯信息

“应用数学和力学·钱伟长讲座”特邀论文

可压缩 Navier-Stokes 方程的时空耦合优化 低维动力系统建模方法*

齐 进¹, 吴锤结²

(1. 北京应用物理与计算数学研究所, 北京 100088;
2. 大连理工大学 航空航天学院, 辽宁 大连 116024)

(本刊编委吴锤结来稿)

摘要: 当采用低维动力系统模型研究 Navier-Stokes 方程的动力学性质时, 保持低维模型的吸引域与 Navier-Stokes 方程的吸引域相同是非常重要的. 然而, 到目前为止, 还没有一种普适的方法能确保对于一般问题都能达到这一目的. 该文发现任何基于空间基的低维模型, 如本征正交分解基、优化空间基和其他经典空间基, 都不具有可预测性, 即低维动力系统的误差随着流场的时间演化而增大. 在构造优化动力系统的理论框架和时空耦合谱展开的新概念下, 该文构造了可压缩 Navier-Stokes 方程的低维模型来逼近大涡模拟方程的数值解, 给出了高精度的流场数值模拟结果和全新的时空耦合基时空演化数值结果. 全场误差在 $10^{-2}\%$ 以下, 而每个网格点的平均误差在 $10^{-8}\%$ 以下. 时空耦合优化低维动力系统可以保证低维模型的吸引域与 Navier-Stokes 方程的吸引域相同. 因此, 保证了时空耦合优化低维动力系统的特征动力学性质与真实流场的特征动力学性质是一致的.

关键词: 时空耦合谱展开; 时空耦合优化低维动力系统; 可压缩 Navier-Stokes 方程; 大涡模拟; 定量比对

中图分类号: O35 文献标志码: A DOI: 10.21656/1000-0887.430220

Construction of Spatiotemporal-Coupling Optimal Low-Dimensional Dynamical Systems for Compressible Navier-Stokes Equations

QI Jin¹, WU Chuijie²

(1. Institute of Applied Physics and Computational Mathematics, Beijing 100088, P.R. China;
2. School of Aeronautics and Astronautics, Dalian University of Technology, Dalian, Liaoning 116024, P.R. China)
(Contributed by WU Chuijie, M. AMM Editorial Board)

Abstract: For the low-dimensional dynamical system model to study dynamics properties of Navier-Stokes equations, it is very important that the attraction domain of the low-dimensional model is the same as that of Navier-Stokes equations. However, to date, there is no universal approach to ensure this purpose for general problems. Herein, it is found that any low-dimensional model based on spatial bases, such as proper orthogonal decomposition bases, optimal spatial bases, and

* 收稿日期: 2022-07-01; 修订日期: 2022-09-30

作者简介: 齐进 (1977—), 女, 副研究员 (E-mail: qi_jin@iapcm.ac.cn);
吴锤结 (1955—), 男, 教授 (通讯作者. E-mail: cjwudut@dlut.edu.cn).

引用格式: 齐进, 吴锤结. 可压缩 Navier-Stokes 方程的时空耦合优化低维动力系统建模方法[J]. 应用数学和力学, 2022, 43(10): 1053-1085.

other classical spatial bases, is not predictable, i.e., the error increases with the time evolution of the flow field. With the theoretical framework for building optimal dynamical systems and the new concept of spatiotemporal-coupling spectrum expansion, the low-dimensional model for compressible Navier-Stokes equations was constructed to approximate the numerical solution to large-eddy simulation equations, and the numerical results and novel time evolution of spatiotemporal-coupling bases were given. The entire field error is typically below $10^{-2}\%$, and the average error at each grid point is below $10^{-8}\%$. The spatiotemporal-coupling optimal low-dimensional dynamical systems can ensure that the attraction domain of the low-dimensional model is the same as that of Navier-Stokes equations. Therefore, characteristic dynamics properties of spatiotemporal-coupling optimal low-dimensional dynamical systems are the same as those of real flow.

Key words: spatiotemporal spectrum expansion; spatiotemporal-coupling optimal low-dimensional dynamical system; compressible Navier-Stokes equations; large-eddy simulation; quantitative comparison

1 Introduction and Overview

1.1 Research Background

For a long time, mathematicians and physicists have been concerned with the solution and research of PDEs (partial differential equations). However, except for a few simple cases, it is very difficult to solve the Navier-Stokes equations. For the general 3D flow problems, the existence and uniqueness of the theoretical solution have not been proven^[1], and it is extremely difficult to study complex flows, such as turbulence.

In the long-term study of turbulence, organized large-scale structures have been found in seemingly disordered flow, i.e., coherent structures, which are composed of vortices with different scales. These coherent structures play a decisive role in the generation and development of turbulence. The study of coherent structures and the establishment and analysis of turbulent low-dimensional dynamical systems are one of the key perspectives to understand the physical essence and law of turbulence.

From the perspective of dynamical system theory, the Navier-Stokes equations belong to an infinite dimensional dynamical system. To study the variation law of its solution with parameters, one of the more feasible methods is to study the nonlinear dynamic characteristics of its low-dimensional dynamical system(LDDS), that is, the dynamical system of infinite-dimensional PDEs is reduced to the finite low-dimensional dynamical system^[2-3], i.e., a set of ordinary differential equations, and the main characteristics of the original system are retained in the finite-dimensional system to the greatest extent. Therefore, for some infinite-dimensional dynamical systems of PDEs, the long-term behaviour and dynamic characteristics can be described and studied in finite-dimensional dynamical systems. This kind of nonlinear dynamic behaviour with the changes of characteristic parameters (including the Reynolds number, Mach number, etc.) plays an important role in the study of complex flows (including the occurrence, development and interaction of instability, turbulence, shock waves, etc.).

In recent years, many researchers^[4-7] have given attention to the modelling and analysis of low-dimensional dynamical systems in turbulence research. Through the Galerkin projection of the Navier-Stokes equations onto a set of suitable bases functions, a low-dimensional dynamical system model consisting of ordinary differential equations with time-varying spectral coefficients was obtained.

1.2 The Construction Methods for Low-Dimensional Dynamical System Models

Dynamical system modelling methods can be divided into the following two categories according to the relationship with PDEs.

1.2.1 The Modelling Method Independent of PDEs

The Galerkin method^[8] based on the Fourier decomposition and the local Taylor expansion^[9] of flow fields are commonly used to build low-dimensional dynamical systems. The modelling method of energy stability analysis^[10-11]

was proposed by Lumley et al., which extracts the flow structure with the largest part of the kinetic energy growth rate, constructs the bases, and then analyses the coherent structure of turbulence.

1.2.2 The Modelling Methods Related to PDEs

① The POD (proper orthogonal decomposition) methods

The essence of this method is to extract the orthogonal bases in the sense of least squares from the numerical simulation or experimental data objectively without prejudice and use the linear combination of fewer bases to approximate and describe the characteristics of the original database and physical process^[12]. Therefore, it is an efficient dimension reduction method.

The application of the POD method can be traced back to the work of Italian geometer Beltrami in 1873 and was first proposed by ref. [13]. It is also called Karkunen-Loève decomposition (in meteorology, it is called the principal component analysis method^[14]). Hofmes and Lumley et al.^[3,10,12,15] introduced the POD method to the study of turbulence for the first time. Through the Galerkin projection of Navier-Stokes equations on the POD bases, a set of low-dimensional models were obtained, and then, the flow characteristics were analysed. However, their low-dimensional models must be built on the known turbulence database, and there are serious problems in the satisfaction of incompressibility and boundary conditions.

It must be pointed out that the POD method has 3 limitations as follow. First, the method is limited to the form of the inner product optimal condition. When the essential characteristics of the system cannot be expressed with the inner product optimal conditions, the method cannot be used to analyse some key regions (including the generation of boundary vorticity flow, etc.) or accurately describe the important flow phenomena at a certain moment (including the dynamic characteristics of vortex breakdown, etc.). Second, due to the existence of projection errors, the low-dimensional dynamical system constructed with the POD method is not necessarily optimal. In the strict sense, this method is only a better means of data processing and analysis. Third, POD bases must be obtained from known databases and cannot be obtained directly from PDEs.

② The OLDDS (optimal low-dimensional dynamical system) theory

To further reduce the dimension and retain the flow field characteristics as much as possible, Wu and Shi^[16-17] proposed the optimization theory for flow database analysis and low-dimensional dynamical systems, which is a more extensive new theory completely different from the POD method. The basic idea of the OLDDS theory is to determine the N -order optimal bases (OBs) to form the N -order intrinsic coordinate system with the methods of optimal control and functional analysis. In this way, the N -order optimal hyperplane derived from this intrinsic coordinate system can approach the exact solution to the infinite-dimensional dynamical system (infinite-dimensional manifold), in the sense of the minimum norm at the parameter value of the studied system, in a wide range of parameters.

Since 1994, the OLDDS theory^[18-23] has been further developed. The flow field structures of a 2D square cavity flow and a backstage step flow were studied, and the Lorenz OLDDS was established to analyse its nonlinear dynamic characteristics. Recently, based on the optimal functional of the minimum weighted residuals, the OLDDS model for the 3D incompressible Navier-Stokes equations^[24] was obtained. For the first time, the authors applied the HWD (helical-wave decomposition) method to the modelling of OLDDS and proposed the generalized HWD-POD OLDDS method of coherent structures^[21], and based on this method, the coherent structures of 3D channel turbulence and the characteristics of its dynamical system were studied. Furthermore, the optimal generalized helical-wave dynamical system of 3D backward-facing step flow was established^[25], and the turbulent elements, i.e., optimal GHWD (generalized helical-wave decomposition) vortices with spatial concentration and slow time-varying characteristics, were obtained.

Recently, the authors and their students developed an OLDDS modelling method for the 3D incompressible

Navier-Stokes equations that satisfies both the arbitrary velocity boundary conditions and the incompressible conditions with the OLDDS modelling method, obtaining the OLDDS model for 3D square cylinder groups (including 1, 2 and 3 square cylinders). Moreover, dynamical system analysis tools (such as the phase space orbit, the Poincaré section, the power spectrum, the Lyapunov exponent set analysis and the bifurcation analysis) were used to analyse the complex dynamical system characteristics of 3D square cylinder groups^[26-28]. It is found that the dynamic characteristics of the wake of a square cylinder are limit cycles. On the other hand, the fluctuating velocity characteristics of the wake of 2 square cylinders are more complicated limit cycles, and the behaviour of the fluctuating OLDDS on its bifurcation diagram is similar to that of period doubling bifurcation, which indicates that more complex dynamic behaviour begins to appear. Based on the dynamical system analysis of OLDDS models (with truncation $N = 10$) of the 3 square cylinder wakes, it is found that the Poincaré section of the wake of 3 square cylinders exhibits chaotic trajectories and broadband power spectra. Through the analysis of its Lyapunov exponent set, it is found that 6 of its 10 Lyapunov exponents are positive, 1 is 0 and 3 are negative, which indicates that the OLDDS behaviour of the wake of 3 square cylinders is chaotic. Thus, it can be seen that in the heat exchanger application, the complexity of the wake can be enhanced by multi-component flow, to promote fluid mixing and improve heat exchange efficiency. It also can be seen that the OLDDS method provides a feasible method to solve the key problems in turbulence research.

It is very difficult to model and analyse the low-dimensional dynamical system of compressible Navier-Stokes equations, there are almost no reports addressing this aspect. The outline of the rest of this paper is as follows. The research objectives are introduced in section 2. The construction theory of spatiotemporal-coupling optimal low-dimensional dynamical system (SCOLDDS) for the general problem is presented in section 3. The construction theory of SCOLDDS for the compressible Navier-Stokes equations is presented in section 4. Applications of SCOLDDS are shown in section 5. Concluding remarks are made in section 6.

2 Research Objectives

To analyse the low-dimensional dynamical system of compressible Navier-Stokes equations, the most important thing is to obtain a suitable low-dimensional dynamical system model which can reflect the characteristics of the original system as much as possible. The modelling method of OLDDS shall satisfy the following 2 conditions:

① Various boundary conditions. However, for complex problems, the usual homogenization cannot be used because it turns one complex problem into another equally complex one. In the Galerkin spectrum method, the basis function that satisfies the boundary conditions is actually a sufficient condition, and it can only be used for periodic boundary conditions and nonslip velocity boundary conditions. Therefore, for the general problem, when the Galerkin spectrum method is used to model the OLDDS and the basis function is still used to satisfy the boundary conditions, the following 2 problems will be encountered: first, for given velocity boundary conditions (such as inflow boundary conditions), how to solve the problem of “1 to many”, i.e., how to assign a velocity boundary condition to N optimal bases; second, how to solve the strong solution boundary condition proposed by unsteady boundary conditions (such as the time-varying outflow boundary condition), given that any spatial basis function can only satisfy the weak solution form of the unsteady boundary condition, that is, it can only satisfy the time-averaging unsteady boundary condition.

② Quantitative comparison to the numerical simulation results of computational fluid dynamics (CFD). The most substantial limitation of the traditional low-dimensional dynamical system modelling method is that, it cannot establish the low-dimensional dynamical system model based on an accurate quantitative comparison with high-dimensional CFD results because only when the dimension of classical spectrum expansion is very large (hundreds

of thousands of dimensions), can it meet the requirement of accurate quantitative comparison. However, the calculation of long-term characteristics of turbulence with high-dimensional dynamical system models is very cumbersome. Therefore, the traditional dynamical system research adopts a very low-dimensional dynamical system model (such as the 3D Lorenz model), but the essential dynamical system characteristics of the low-dimensional model are likely to be completely different from those of the real turbulence (that is, they are in different regions of the functional space).

Therefore, it is necessary to extend the OLDDES modelling theory. In this paper, a SCOLDDS modelling method was proposed to obtain a SCOLDDS model for compressible Navier-Stokes equations that satisfies various complex geometrical and physical boundary conditions and can be quantitatively compared with high-dimensional numerical simulation results.

The SCOLDDS of turbulence established based on an accurate quantitative comparison is not only in the same region of functional space as the real turbulence dynamical system but its SCOBs (spatiotemporal-coupling optimal bases) are also coherent structures, and the intrinsic optimal bases are very low-dimensional (such as the 3rd-order SCOBs used in this study); therefore, the very low-dimensional SCOLDDS can be obtained, which can greatly reduce the amount of calculation in the study of long-term characteristics of turbulent dynamical systems.

3 The Construction Theory of SCOLDDS for General Problem

3.1 The Basic Idea and the Essential Innovation of Optimal Bases

The basic idea of the OLDDES theory for PDEs is shown in [fig. 1](#); i.e., with the methods of optimal control and functional analysis, the N -order intrinsic coordinate system composed of N -order optimal bases is obtained so that the N -order optimal hyperplane constructed from the N -order intrinsic coordinate system can approach the exact solution to the infinite-dimensional dynamical system (infinite-dimensional manifold) well in the sense of the minimum norm at the parameter value of the studied system and in a wide range of parameters.

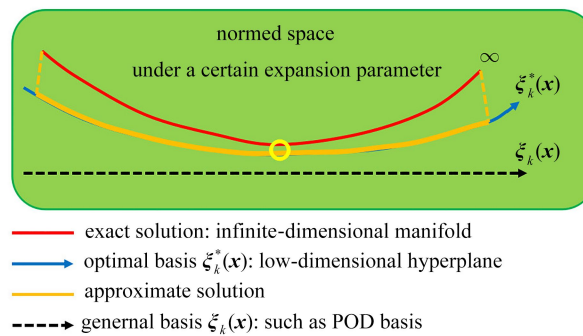


Fig. 1 The basic idea of the OLDDES theory

Note To get the meanings of different colors in the figure, the readers could refer to the electronic webpage of this article.

The most substantial difference between the N -order optimal bases and the traditional spectral expansion is that in the spectral expansion $\mathbf{u}(x, t) \approx \sum_{k=1}^N a_k(t) \xi_k$ of system variables $\mathbf{u}(x, t)$, optimal bases ξ_k^* are not given in advance, and the N -order optimal bases that depend on the given differential equations and initial and boundary conditions are obtained with the optimal control method under the condition of satisfying the quantitative comparison, the given optimal functional and other constraints. The low-dimensional dynamical system model based on the optimal bases ξ_k^* is an OLDDES.

The starting point of the theory of low-dimensional dynamical systems for PDEs is spectral expansion:

$$\mathbf{u}(x, t) = \sum_{k=1}^{\infty} a_k(t) \xi_k = \mathbf{u}_N + \mathbf{u}_R \approx \mathbf{u}_N = \sum_{k=1}^N a_k(t) \xi_k, \tag{1}$$

where \mathbf{u}_R is the remainder, N is the order of spectral expansion, ξ_k are basis functions, also called spectral functions. For classical spectral expansion, ξ_k are known spatial bases, i.e., $\xi_k = \xi_k(\mathbf{x})$. For optimal bases, $\xi_k = \xi_k^*(\mathbf{x})$ are not given in advance. The N -order optimal bases that depend on the given differential equations and initial and boundary conditions are obtained with the optimal control method under the condition of satisfying the given optimal function and other constraints.

The essential innovation of the theory of SCOLDDS proposed in this paper is that the basis functions are N -order optimal bases ξ_k^* related to physical problems, and if the SCOBs are used to represent the spatiotemporal-coupling characteristics of the system, they are SCOBs $\xi_k = \xi_k^*(\mathbf{x}, t)$, or if the time-averaged characteristic of the system is represented by the spatial optimal bases, they are optimal spatial bases $\xi_k = \xi_k^*(\mathbf{x})$.

Because the snapshot POD bases must satisfy the ergodic condition of each state, period T cannot be too small, so the real-time spatiotemporal-coupling POD bases cannot be obtained. On the other hand, because all spatiotemporal flow data must be used to find the POD bases, when T is very large, the amount of calculation of POD will be too high, so the full time-space POD bases cannot be obtained. Therefore, it is impossible to obtain the SCOLDDS model based on POD bases.

3.2 The Mathematical Problem and the Construction of Low-Dimensional Models

3.2.1 The Mathematical Problem

For the initial boundary value problem of general PDEs, whose governing equations, initial conditions and boundary conditions are as follow:

$$\begin{cases} \frac{\partial \mathbf{u}}{\partial t} + L(\mathbf{u}) = 0, & \mathbf{x} \in \Omega, t > 0, \\ \mathbf{u}(\mathbf{x}, 0) = \mathbf{u}_0(\mathbf{x}), & \mathbf{x} \in \Omega, \\ [\alpha \mathbf{u} + \beta \nabla \mathbf{u} \cdot \mathbf{n}]_{\partial \Omega} = \mathbf{g}(\mathbf{x}, t), & \mathbf{x} \in \partial \Omega, t > 0, \end{cases} \tag{2}$$

where \mathbf{n} is the normal direction of the boundary, and $\mathbf{g}(\mathbf{x}, t)$ are values at boundaries.

Suppose that the problem is studied in the Sobolev space^[29] with norm, i.e.,

$$\mathbf{u}(\mathbf{x}, t) \in \mathcal{W}^{m,p}(\Omega_T), \tag{3}$$

where $\Omega_T = \Omega \times [0, T]$, indexes m and p depend on the smoothness of \mathbf{u} ; $p = 2q$, $m, q \in \mathbb{N}$, \mathbb{N} are sets of all positive integers. The norm in the Sobolev space is defined as

$$\|\mathbf{u}\|_{\mathcal{W}^{m,p}(\Omega_T)} = \left(\sum_{|\alpha| \leq m} \|D^\alpha \mathbf{u}\|_{\mathcal{L}^p(\Omega_T)^p} \right)^{1/p}, \tag{4}$$

where $D^\alpha \mathbf{u}$ is a generalized difference of order α , and $\mathcal{L}^p(\Omega_T)$ is the set of all (p) integrable functions in Ω_T ; if $\mathbf{u} = (u_1, u_2, \dots, u_N)^T$, then

$$\|\mathbf{u}\|_{\mathcal{L}^p(\Omega_T)} = \left(\int_{\Omega_T} \sum_{k=1}^N u_k^p d\Omega dt \right)^{1/p}. \tag{5}$$

The following defines basis functions $\xi_k (k = 1, 2, \dots, \infty)$ in the Sobolev space as follows, and expanded space \mathcal{B} satisfying the following conditions:

$$\mathcal{B} = \{[\xi_k]_{k=1}^\infty | \mathbf{x} \in \Omega \subset \mathbb{R}^n, \xi_k \in \mathcal{W}^{m,p}(\Omega)\}. \tag{6}$$

Hence, suppose that exact solution $\mathbf{u}(\mathbf{x}, t)$ of eq. (2) can be expressed as an infinite-dimensional weak solution in the space \mathcal{B} as follows:

$$\mathbf{u}(\mathbf{x}, t) = \sum_{k=1}^\infty a_k(t) \xi_k. \tag{7}$$

Next, further limit the problem to the Hilbert space^[30] $\mathcal{H}^\infty(\Omega)$ with inner products, and let basis functions satisfy the orthogonality condition, one can define expanded functional space \mathcal{B} as

$$\mathcal{B} = \{[\xi_k]_{k=1}^\infty | \mathbf{x} \in \Omega \subset \mathbb{R}^n, \xi_k \in \mathcal{H}^\infty(\Omega), (\xi_k, \xi_l) = \delta_{kl}\}, \tag{8}$$

where (\cdot) expresses the inner products in $\mathcal{H}^\infty(\Omega)$, i.e.,

$$(\xi_k, \xi_l) = \int_\Omega \xi_k \cdot \xi_l d\Omega. \tag{9}$$

These forms correspond to infinite-dimensional dynamical systems.

3.2.2 The Construction of Low-Dimensional Models

Next, further limit the problem to the N -order Hilbert space^[30] $\mathcal{H}^N(\Omega)$ with inner products, and let basis functions satisfy the orthogonality condition, one can define expanded functional space \mathcal{B}_N as

$$\mathcal{B}_N = \{[\xi_k]_{k=1}^N | \mathbf{x} \in \Omega \subset \mathbb{R}^n, \xi_k \in \mathcal{H}^N(\Omega), (\xi_k, \xi_l) = \delta_{kl}\}, \tag{10}$$

where (\cdot) expresses the L^2 inner products in $\mathcal{H}^N(\Omega)$, i.e.,

$$(\xi_k, \xi_l) = \int_\Omega \xi_k \cdot \xi_l d\Omega. \tag{11}$$

The first N items of extraction formula eq. (7) are truncated to obtain low-dimensional approximate spectral expansion $\mathbf{u}(\mathbf{x}, t)$ in \mathcal{B}_N as

$$\mathbf{u}(\mathbf{x}, t) = \mathbf{u}_N(\mathbf{x}, t) + \mathbf{u}_R(\mathbf{x}, t) \approx \mathbf{u}_N(\mathbf{x}, t) = \sum_{k=1}^N a_k(t) \xi_k, \tag{12}$$

where $\mathbf{u}_R(\mathbf{x}, t)$ is the remainder, $a_k(t)$ and ξ_k ($k = 1, 2, \dots, N, \dots$, the same below) are all unknown functions that depend on specific problems satisfying

$$a_k = (\mathbf{u}, \xi_k). \tag{13}$$

Substituting eq. (12) into eq. (2) and projecting it onto basis ξ_k , one obtains Galerkin projection equation^[2] G_k^p as follows:

$$G_k^p = \left(\frac{\partial \mathbf{u}_N}{\partial t} + L(\mathbf{u}_N), \xi_k \right) = 0. \tag{14}$$

The Galerkin projection equation is a low-dimensional model for eq. (2), that is, a low-dimensional dynamical system, which are ordinary differential equations of $a_k(t)$, and have the following form:

$$a_{k,t}(t) = f(a_k, \xi_k, \nabla \xi_k, \dots), \tag{15}$$

where subscript “ t ” denotes the derivative with respect to time. Thus, the dimensionality reduction approximation of eq. (2) is realized. It is noted that dimension D of a dynamical system is defined as order of spectral expansion N times number of independent flow variables M .

The low-dimensional dynamical system model is based on the optimal bases ξ_k^* .

3.2.3 The Optimal Problem of Obtaining the Optimal Basis

It is necessary to conduct a reasonable analysis and assumption of the physical problem and put forward the appropriate optimal conditions, and construct optimal objective functional $J(\xi_k)$; then, the construction of OLDDES is reduced to the following optimization problem:

$$\begin{cases} \min & J(\xi_k), \\ \text{s.t.} & G_k^p(a_k, \xi_k) = 0, \\ & \xi_k \in \mathcal{B}_N, \end{cases} \tag{16}$$

where $G_k^p(a_k, \xi_k) = 0$ shows that eq. (14) consists of the functions of a_k and ξ_k .

From eq. (16), it can be seen that given generalized optimal objective functional $J(\xi_k)$, the key to constructing the OLDDES is to obtain optimal basis ξ_k^* . Therefore, various optimization methods can be used to obtain the optimal basis, including the conjugate gradient local optimization algorithm, local optimization programs such as conmax, and global optimization algorithms such as genetic algorithms and deep learning methods, etc.

Next, the specific method of conjugate gradient optimization is introduced. The following two sets of equations

can be obtained through variational operation of objective functional J and let $\nabla J^g = 0$:

$$a_{k,t} = f(a_k, \xi_k, \nabla \xi_k, \dots), \tag{17a}$$

$$\nabla J^g = \sum_{k=1}^N \frac{\partial J_k^g}{\partial \xi_k} = 0, \tag{17b}$$

where J_k^g is the k th component of generalized optimal objective functional J^g , which is called the Hamiltonian function^[31]. Optimal basis ξ_k^* can be obtained when eq. (17) is solved simultaneously.

Next, the 2 sets of equations in eq. (17) are explained.

① Ordinary differential eq. (17a) of $a_k(t)$: it is the OLDDS equation, which contains the complex nonlinear dynamical characteristics (such as chaos), and the initial conditions for solving the equation are $a_k(0) = (\mathbf{u}_0, \xi_k)$.

② Generalized optimal objective functional ∇J^g gradient eq. (17b): for the equations of basis functions ξ_k , gradient ∇J^g of the generalized optimal objective functional is defined as

$$J^g(\xi_k + \delta \xi_k) - J^g(\xi_k) \equiv \int_{\Omega} \nabla J^g \cdot \delta \xi_k \, d\Omega + O(\|\delta \xi_k\|). \tag{18}$$

The solution to equation ξ_k^* yields the optimal basis. On the one hand, the optimal basis are used to construct the OLDDS; on the other hand, the solution can achieve the best approximation of the exact solution of eq. (2), which reflects the mathematical characteristics of eq. (2) with physical significance. It is worth noting that due to the effect of boundary conditions, the equations of the functional gradient in Ω and at boundary $\partial\Omega$ are different, and different equations are provided for different boundary conditions.

4 The Construction Theory of SCOLDDS for Compressible Navier-Stokes Equations

4.1 Compressible Navier-Stokes Equations

In Cartesian coordinates, the dimensionless 3D unsteady compressible Navier-Stokes equations^[32] (including the continuity equation, the momentum equation, the energy equation, the state equation, and the initial and boundary conditions, with the exception of hypersonic flow, i.e., regardless of the ionizing radiation of a fluid) are considered:

$$\begin{cases} \rho_{,t} + (\rho u_j)_{,j} = 0, \\ (\rho u_i)_{,t} + \left(\rho u_i u_j + \frac{p}{\gamma Ma^2} \delta_{ij} \right)_{,j} = \frac{1}{Fr^2} \rho f_i + \frac{1}{Re} \sigma_{ij,j}, \\ E_{,t} + \left[\left(E + \frac{p}{\gamma Ma^2} \right) u_j \right]_{,j} = \frac{1}{\alpha} (\kappa T_{,j})_{,j} + \frac{1}{Re} (\sigma_{ij} u_i)_{,j}, \\ p = \rho T, \\ (u_i, \rho, E, T) = (u_i, \rho, E, T)|_{t=0}, \\ (\rho, \rho_{,j} n_j)_{\partial\Omega} = (\rho_B, \rho_{B,j} n_j), \\ (u_i, u_{i,j} n_j)_{\partial\Omega} = (u_{Bi}, u_{Bi,j} n_j), \\ (T, T_{,j} n_j)_{\partial\Omega} = (T_B, T_{B,j} n_j), \end{cases} \tag{19}$$

where the initial conditions and boundary conditions are determined according to specific problems, and the variables with subscripts B are their boundary values, ρ , p and T are the dimensionless density, pressure and temperature, respectively, u_i is the dimensionless velocity field, and f_i is the dimensionless mass force. Here, the ideal gas model is used for the thermodynamics relationship, and it can be seen from ref. [33] that the state equation of an ideal gas is $p = \rho R_g T$, $R_g = \frac{R}{\tilde{M}}$, where R is a universal gas constant that is independent of gas type and gas constant R_g is related to gas type, and \tilde{M} is the Molar mass of the gas. Specific heat ratio $\gamma \equiv c_p/c_v$ is set equal to 1.4, where c_p and c_v are the isobaric specific heat and isochoric specific heat, respectively. The 4 control parameters are defined as: characteristic Froude number $Fr \equiv \frac{U_\infty}{\sqrt{g_\infty L_\infty}}$, characteristic Prandtl number $Pr \equiv \mu_\infty \gamma R_g / [(\gamma - 1) \kappa_\infty]$,

characteristic Reynolds number $Re \equiv \rho_\infty U_\infty L_\infty / \mu_\infty$ and characteristic Mach number $Ma \equiv U_\infty / c_\infty$. The characteristic Prandtl number is $Pr = 0.72$, and parameter α is defined as $\alpha \equiv Pr Re (\gamma - 1) Ma^2$. Dimensionless viscous stress tensor σ_{ij} and dimensionless total energy E are defined as

$$\sigma_{ij} \equiv \mu(u_{i,j} + u_{j,i}) - \frac{2}{3} \mu \theta \delta_{ij}, \tag{20}$$

$$E \equiv \frac{p}{(\gamma - 1) \gamma Ma^2} + \frac{1}{2} \rho (u_h u_h), \tag{21}$$

where $\theta = u_{i,i}$ is the dimensionless velocity divergence.

In compressible turbulence, it is necessary to consider the influence of temperature change on dynamic viscosity coefficient μ and heat conduction coefficient κ [34], i.e.,

$$\mu = \frac{1.4049 \bar{T}^{1.5}}{\bar{T} + 0.4049}, \tag{22}$$

$$\kappa = \frac{1.4049 \bar{T}^{1.5}}{\bar{T} + 0.4049}. \tag{23}$$

From ref. [35], one can see that temperature \bar{T} in Sutherland's formula is a spatially averaged temperature; therefore, in the modelling of the SCOLDDS and the dynamical system analysis, let μ and κ be constants, their values is determined the spatial-average initial temperature \bar{T}_∞ from eq. (22) and eq. (23). After the whole calculation, for the case in which the values of all variables are obtained in the whole flow field, temperature field $T(\mathbf{x}, t)$ at different moments is substituted into Sutherland formula eq. (22) and eq. (23) to obtain the approximate spatiotemporal distribution values of $\mu(\mathbf{x}, t)$ and $\kappa(\mathbf{x}, t)$. It must be pointed out that these approximate spatiotemporal distribution values of $\mu(\mathbf{x}, t)$ and $\kappa(\mathbf{x}, t)$ obtained after the completion of the whole calculation have no influence on the results of the fluid field calculation and the dynamical system analysis.

Let $p = \rho T$, $\theta = u_{i,i}$, $\alpha \equiv Pr Re (\gamma - 1) Ma^2$, eq. (20) and eq. (21) be introduced into eq. (19); then, 5 scalar governing equations (including the continuity equation, 3 scalar momentum equations and the energy equation) of compressible flow are obtained, through which 5 flow variables can be obtained (including ρ, T, u_j):

$$\left\{ \begin{array}{l} \rho_{,t} + (\rho u_j)_{,j} = 0, \\ (\rho u_i)_{,t} + \left(\rho u_i u_j + \frac{\rho T}{\gamma Ma^2} \delta_{ij} \right)_{,j} = \frac{1}{Fr^2} \rho f_i + \frac{\mu}{Re} \left[(u_{i,j} + u_{j,i}) - \frac{2}{3} u_{h,h} \delta_{ij} \right]_{,j}, \\ \left[\frac{\rho T}{(\gamma - 1) \gamma Ma^2} + \frac{1}{2} \rho (u_h u_h) \right]_{,t} + \left\{ \left[\frac{\rho T}{(\gamma - 1) \gamma Ma^2} + \frac{1}{2} \rho (u_h u_h) + \frac{\rho T}{\gamma Ma^2} \right] u_j \right\}_{,j} = \\ \frac{\kappa}{Pr Re (\gamma - 1) Ma^2} T_{,jj} + \frac{\mu}{Re} \left\{ \left[(u_{i,j} + u_{j,i}) - \frac{2}{3} u_{h,h} \delta_{ij} \right] u_i \right\}_{,j}, \\ (u_i, \rho, T) = (u_i, \rho, T)|_{t=0}, \\ (\rho, \rho_{,j} n_j)_{\partial\Omega} = (\rho_B, \rho_{B,j} n_j), \\ (u_i, u_{i,j} n_j)_{\partial\Omega} = (u_{Bi}, u_{Bi,j} n_j), \\ (T, T_{,j} n_j)_{\partial\Omega} = (T_B, T_{B,j} n_j). \end{array} \right. \tag{24}$$

4.2 Spatiotemporal-Coupling Low-Dimensional Dynamical Systems for Compressible Navier-Stokes Equations and Numerical Realization of Boundary Conditions

4.2.1 Spatiotemporal-Coupling Low-Dimensional Dynamical Systems for Compressible Navier-Stokes Equations

The SCOLDDS modelling theory in section 3 are applied to the compressible Navier-Stokes equations to derive the SCOLDDS equations.

Define functional spaces \mathcal{B}_N^u , \mathcal{B}_N^p and \mathcal{B}_N^T to satisfy conditions:

$$\left\{ \begin{aligned} \mathcal{B}_N^p &= \left\{ [\zeta_k]_{k=1}^N \mid \zeta_k \in \mathcal{H}^N(\Omega), \int_{\Omega} \zeta_k \zeta_l \, d\Omega = \delta_{kl}, \text{ and } \zeta_k \text{ second-order differentiable} \right\}, \\ \mathcal{B}_N^u &= \left\{ [\xi_{ki}]_{k=1}^N \mid \xi_{ki} \in \mathcal{H}^N(\Omega), \int_{\Omega} \xi_{ki} \xi_{li} \, d\Omega = \delta_{kl}, \text{ and } \xi_{ki} \text{ second-order differentiable} \right\}, \\ \mathcal{B}_N^T &= \left\{ [\eta_k]_{k=1}^N \mid \eta_k \in \mathcal{H}^N(\Omega), \int_{\Omega} \eta_k \eta_l \, d\Omega = \delta_{kl}, \text{ and } \eta_k \text{ second-order differentiable} \right\}. \end{aligned} \right. \tag{25}$$

Express u_i, ρ and T in compressible Navier-Stokes equations eq. (24) by following low-dimensional approximations in functional spaces $\mathcal{B}_N^u, \mathcal{B}_N^p$ and \mathcal{B}_N^T , respectively:

$$\left\{ \begin{aligned} \rho &= b_k \zeta_k + \rho_R \approx b_k \zeta_k, \\ u_i &= a_k \xi_{ki} + u_{Ri} \approx a_k \xi_{ki}, \\ T &= c_k \eta_k + T_R \approx c_k \eta_k, \end{aligned} \right. \tag{26}$$

where expansion order N is omitted and left unwritten, similarly hereinafter. With the mass force omitted and eq. (26) substituted into eq. (24), the low-dimensional truncated compressible Navier-Stokes equations expressed by the N th basis are obtained as follow:

$$\left\{ \begin{aligned} & b_{l,i} \zeta_l + b_l a_k (\zeta_l \xi_{kj})_{,j} = 0, \\ & (b_l a_k)_{,i} \zeta_l \xi_{ki} + b_l a_k a_m (\zeta_l \xi_{ki} \xi_{mj})_{,j} + \frac{1}{\gamma Ma^2} b_l c_m (\zeta_l \eta_m \delta_{ij})_{,j} - \\ & \quad \frac{\mu}{Re} \left[a_k \xi_{ki,j} + a_k \xi_{kj,i} - \frac{2}{3} a_l (\xi_{lh,h} \delta_{ij}) \right]_{,j} = 0, \\ & (b_l c_m)_{,i} \frac{1}{(\gamma - 1) \gamma Ma^2} \zeta_l \eta_m + \frac{1}{2} (b_l a_k a_m)_{,i} \zeta_l \xi_{kh} \xi_{mh} + \\ & \quad \left[\left(\frac{1}{(\gamma - 1) \gamma Ma^2} b_l \zeta_l c_m \eta_m + \frac{1}{2} b_l \zeta_l a_k \xi_{kh} a_m \xi_{mh} + \frac{1}{\gamma Ma^2} b_l \zeta_l c_m \eta_m \right) a_n \xi_{nj} \right]_{,j} - \\ & \quad \frac{\kappa}{Pr Re (\gamma - 1) Ma^2} c_n \eta_{n,jj} - \frac{\mu}{Re} \left[\left(a_k \xi_{ki,j} + a_k \xi_{kj,i} - \frac{2}{3} a_l \xi_{lh,h} \delta_{ij} \right) a_n \xi_{ni} \right]_{,j} = 0, \\ & (a_k \xi_{ki}, b_l \zeta_l, c_m \eta_m) = (u_{0i}, \rho_0, T_0), \\ & (b_k \zeta_k, b_k \zeta_{k,j} n_j)_{\partial\Omega} = (\rho_B, \rho_{B,j} n_j), \\ & (a_k \xi_{ki}, a_k \xi_{ki,j} n_j)_{\partial\Omega} = (u_{Bi}, u_{Bi,j} n_j), \\ & (c_k \eta_k, c_k \eta_{k,j} n_j)_{\partial\Omega} = (T_B, T_{B,j} n_j). \end{aligned} \right. \tag{27}$$

To satisfy the boundary conditions in the equations of a low-dimensional dynamical system, the approximate density field, velocity field and temperature field satisfying the boundary conditions are introduced, respectively,

$$\mathcal{U}_i = \begin{cases} a_k \xi_{ki}, & \text{in } \Omega \setminus \partial\Omega, \\ (a_k \xi_{ki})^{bd}, & \text{on } \partial\Omega, \end{cases} \tag{28}$$

$$\mathcal{D} = \begin{cases} b_k \zeta_k, & \text{in } \Omega \setminus \partial\Omega, \\ (b_k \zeta_k)^{bd}, & \text{on } \partial\Omega, \end{cases} \tag{29}$$

$$\mathcal{T} = \begin{cases} c_k \eta_k, & \text{in } \Omega \setminus \partial\Omega, \\ (c_k \eta_k)^{bd}, & \text{on } \partial\Omega, \end{cases} \tag{30}$$

where the specific forms of $(a_k \xi_{ki})^{bd}, (b_k \zeta_k)^{bd}$ and $(c_k \eta_k)^{bd}$ are determined by the boundary conditions, respectively, and the specific implementation process is shown in section 4.2.2.

Next, by the boundary condition treatment, the specific form of Galerkin projection equations of the continuity equation, momentum equation and energy equation in eq. (27) is derived to obtain the dynamical system equations for compressible Navier-Stokes equations.

① The Galerkin projection of the continuity equation on arbitrary density basis ζ_r

The Galerkin projection of the continuity equation (the 1st equation in eq. (27)) on arbitrary density bases ζ_r is

$$G_r^{pp} = (b_{l,i} \zeta_l, \zeta_r) + (b_l a_k (\zeta_l \xi_{kj})_{,j}, \zeta_r). \tag{31}$$

The derivation of each term of eq. (31) is as follows:

$$(b_{l,t}\zeta_l, \zeta_r) = b_{r,t}, \tag{32}$$

$$(b_l a_k (\zeta_l \xi_{kj})_{,j}, \zeta_r) = b_l a_k \int_{\Omega} \zeta_l \xi_{kj} \zeta_r \, d\Omega + b_l a_k \int_{\Omega} \zeta_l \xi_{kj} \zeta_r \, d\Omega = \int_{\Omega} \mathcal{D}\mathbf{U}_{j,j} \zeta_r \, d\Omega + \int_{\Omega} \mathcal{D}_{,j} \mathbf{U}_j \zeta_r \, d\Omega. \tag{33}$$

Therefore, the Galerkin projection expression of the continuity equation on arbitrary density basis ζ_r is obtained:

$$G_r^{p\rho} = b_{r,t} + \int_{\Omega} \mathcal{D}\mathbf{U}_{j,j} \zeta_r \, d\Omega + \int_{\Omega} \mathcal{D}_{,j} \mathbf{U}_j \zeta_r \, d\Omega. \tag{34}$$

② The Galerkin projection of the momentum equation on arbitrary velocity basis ξ_{ri}

The Galerkin projection of the momentum equation (the 2nd equation in eq. (27)) on arbitrary velocity basis ξ_{ri} is

$$G_r^{pu} = ((b_l a_k)_{,t} \zeta_l \xi_{ki}, \xi_{ri}) + (b_l a_k a_m (\zeta_l \xi_{ki} \xi_{mj})_{,j}, \xi_{ri}) + \frac{1}{\gamma Ma^2} b_l c_m ((\zeta_l \eta_m \delta_{ij})_{,j}, \xi_{ri}) - \frac{\mu}{Re} \left\{ \left[a_k \xi_{ki,j} + a_k \xi_{kji} - \frac{2}{3} a_l (\xi_{lh,h} \delta_{ij}) \right]_{,j}, \xi_{ri} \right\}. \tag{35}$$

The derivation of each item in eq. (35) is as follows:

$$((b_l a_k)_{,t} \zeta_l \xi_{ki}, \xi_{ri}) = b_l a_{k,t} \int_{\Omega} \zeta_l \xi_{ki} \xi_{ri} \, d\Omega + b_{l,t} a_k \int_{\Omega} \zeta_l \xi_{ki} \xi_{ri} \, d\Omega = a_{k,t} \int_{\Omega} \mathcal{D}\xi_{ki} \xi_{ri} \, d\Omega + b_{l,t} \int_{\Omega} \zeta_l \mathbf{U}_i \xi_{ri} \, d\Omega, \tag{36}$$

$$(b_l a_k a_m (\zeta_l \xi_{ki} \xi_{mj})_{,j}, \xi_{ri}) + \frac{1}{\gamma Ma^2} b_l c_m ((\zeta_l \eta_m \delta_{ij})_{,j}, \xi_{ri}) = b_l a_k a_m \int_{\Omega} (\zeta_l \xi_{ki} \xi_{mj})_{,j} \xi_{ri} \, d\Omega + \frac{1}{\gamma Ma^2} b_l c_m \int_{\Omega} (\zeta_l \eta_m \delta_{ij})_{,j} \xi_{ri} \, d\Omega = \int_{\Omega} (\mathcal{D}\mathbf{U}_i \mathbf{U}_j)_{,j} \xi_{ri} \, d\Omega + \frac{1}{\gamma Ma^2} \int_{\Omega} (\mathcal{D}\mathcal{T} \delta_{ij})_{,j} \xi_{ri} \, d\Omega, \tag{37}$$

$$\frac{\mu}{Re} \left\{ \left[a_k \xi_{ki,j} + a_k \xi_{kji} - \frac{2}{3} a_l (\xi_{lh,h} \delta_{ij}) \right]_{,j}, \xi_{ri} \right\} = -\frac{\mu}{Re} \int_{\Omega} \left(a_k \xi_{ki,j} + a_k \xi_{kji} - \frac{2}{3} a_l (\xi_{lh,h} \delta_{ij}) \right)_{,j} \xi_{ri} \, d\Omega = -\frac{\mu}{Re} \int_{\Omega} \left(\mathbf{U}_{i,j} + \mathbf{U}_{j,i} - \frac{2}{3} \mathbf{U}_{h,h} \delta_{ij} \right)_{,j} \xi_{ri} \, d\Omega. \tag{38}$$

Therefore, the Galerkin projection expression of the momentum equation on arbitrary velocity bases ξ_{ri} is obtained as follows:

$$G_r^{pu} = a_{k,t} \int_{\Omega} \mathcal{D}\xi_{ki} \xi_{ri} \, d\Omega + b_{l,t} \int_{\Omega} \zeta_l \mathbf{U}_i \xi_{ri} \, d\Omega + \int_{\Omega} (\mathcal{D}\mathbf{U}_i \mathbf{U}_j)_{,j} \xi_{ri} \, d\Omega + \frac{1}{\gamma Ma^2} \int_{\Omega} (\mathcal{D}\mathcal{T} \delta_{ij})_{,j} \xi_{ri} \, d\Omega - \frac{\mu}{Re} \int_{\Omega} \left(\mathbf{U}_{i,j} + \mathbf{U}_{j,i} - \frac{2}{3} \mathbf{U}_{h,h} \delta_{ij} \right)_{,j} \xi_{ri} \, d\Omega. \tag{39}$$

③ The Galerkin projection of the energy equation (the 3rd equation in eq. (27)) on arbitrary temperature basis η_r is

$$G_r^{pT} = (b_l c_m)_{,t} \frac{1}{(\gamma - 1) \gamma Ma^2} (\zeta_l \eta_m, \eta_r) + \frac{1}{2} (b_l a_k a_m)_{,t} (\zeta_l \xi_{kh} \xi_{mh}, \eta_r) + \left\{ \left[\left(\frac{1}{(\gamma - 1) \gamma Ma^2} b_l \zeta_l c_m \eta_m + \frac{1}{2} b_l \zeta_l a_k \xi_{kh} a_m \xi_{mh} + \frac{1}{\gamma Ma^2} b_l \zeta_l c_m \eta_m \right) a_n \xi_{nj} \right]_{,j}, \eta_r \right\} - \frac{\kappa}{Pr Re (\gamma - 1) Ma^2} c_n (\eta_{n,jj}, \eta_r) - \frac{\mu}{Re} \left\{ \left[\left(a_k \xi_{ki,j} + a_k \xi_{kji} - \frac{2}{3} a_l \xi_{lh,h} \delta_{ij} \right) a_n \xi_{ni} \right]_{,j}, \eta_r \right\}. \tag{40}$$

The projection of each item in eq. (40) on arbitrary temperature basis η_r is deduced as follows:

$$\begin{aligned}
 (b_l c_m)_{,t} \frac{1}{(\gamma-1)\gamma Ma^2} (\zeta_l \eta_m, \eta_r) = & \\
 \frac{1}{(\gamma-1)\gamma Ma^2} c_{m,t} b_l \int_{\Omega} \zeta_l \eta_m \eta_r \, d\Omega + \frac{1}{(\gamma-1)\gamma Ma^2} c_m b_{l,t} \int_{\Omega} \zeta_l \eta_m \eta_r \, d\Omega = & \\
 \frac{1}{(\gamma-1)\gamma Ma^2} c_{m,t} \int_{\Omega} \mathcal{D} \eta_m \eta_r \, d\Omega + \frac{1}{(\gamma-1)\gamma Ma^2} b_{l,t} \int_{\Omega} \zeta_l \mathcal{T} \eta_r \, d\Omega, & \quad (41)
 \end{aligned}$$

$$\begin{aligned}
 \frac{1}{2} (b_l a_k a_m)_{,t} (\zeta_l \xi_{kh} \xi_{mh}, \eta_r) = & \\
 \frac{1}{2} (b_l a_k a_m)_{,t} \int_{\Omega} \zeta_l \xi_{kh} \xi_{mh} \eta_r \, d\Omega = & \\
 \frac{1}{2} b_{l,t} \int_{\Omega} \zeta_l \mathbf{u}_h \mathbf{u}_h \eta_r \, d\Omega + \frac{1}{2} a_{k,t} \int_{\Omega} \mathcal{D} \xi_{kh} \mathbf{u}_h \eta_r \, d\Omega + \frac{1}{2} a_{m,t} \int_{\Omega} \mathcal{D} \mathbf{u}_h \xi_{mh} \eta_r \, d\Omega = & \\
 \frac{1}{2} b_{l,t} \int_{\Omega} \zeta_l \mathbf{u}_h \mathbf{u}_h \eta_r \, d\Omega + a_{k,t} \int_{\Omega} \mathcal{D} \xi_{kh} \mathbf{u}_h \eta_r \, d\Omega, & \quad (42)
 \end{aligned}$$

$$\begin{aligned}
 \left\{ \left[\left(\frac{1}{(\gamma-1)\gamma Ma^2} b_l \zeta_l c_m \eta_m + \frac{1}{2} b_l \zeta_l a_k \xi_{kh} a_m \xi_{mh} + \frac{1}{\gamma Ma^2} b_l \zeta_l c_m \eta_m \right) a_n \xi_{nj} \right]_{,j}, \eta_r \right\} = & \\
 \frac{1}{(\gamma-1)\gamma Ma^2} b_l c_m a_n \int_{\Omega} (\zeta_l \eta_m \xi_{nj})_{,j} \eta_r \, d\Omega + \frac{1}{2} b_l a_k a_m a_n \int_{\Omega} (\zeta_l \xi_{kh} \xi_{mh} \xi_{nj})_{,j} \eta_r \, d\Omega + & \\
 \frac{1}{\gamma Ma^2} b_l c_m a_n \int_{\Omega} (\zeta_l \eta_m \xi_{nj})_{,j} \eta_r \, d\Omega = & \\
 \frac{1}{(\gamma-1)\gamma Ma^2} \int_{\Omega} (\mathcal{D} \mathcal{T} \mathbf{u}_j)_{,j} \eta_r \, d\Omega + \frac{1}{2} \int_{\Omega} (\mathcal{D} \mathbf{u}_h \mathbf{u}_h \mathbf{u}_j)_{,j} \eta_r \, d\Omega + & \\
 \frac{1}{\gamma Ma^2} \int_{\Omega} (\mathcal{D} \mathcal{T} \mathbf{u}_j)_{,j} \eta_r \, d\Omega = & \\
 \frac{1}{(\gamma-1)Ma^2} \int_{\Omega} (\mathcal{D} \mathcal{T} \mathbf{u}_j)_{,j} \eta_r \, d\Omega + \frac{1}{2} \int_{\Omega} (\mathcal{D} \mathbf{u}_h \mathbf{u}_h \mathbf{u}_j)_{,j} \eta_r \, d\Omega, & \quad (43)
 \end{aligned}$$

$$\begin{aligned}
 \frac{\kappa}{PrRe(\gamma-1)Ma^2} c_n (\eta_{n,jj}, \eta_r) = & \\
 - \frac{\kappa}{PrRe(\gamma-1)Ma^2} c_n \int_{\Omega} \eta_{n,jj} \eta_r \, d\Omega = - \frac{\kappa}{PrRe(\gamma-1)Ma^2} \int_{\Omega} \mathcal{T}_{,jj} \eta_r \, d\Omega, & \quad (44)
 \end{aligned}$$

$$\begin{aligned}
 \frac{\mu}{Re} \left\{ \left[\left(a_k \xi_{ki,j} + a_k \xi_{kji} - \frac{2}{3} a_l \xi_{lh,h} \delta_{ij} \right) a_n \xi_{ni} \right]_{,j}, \eta_r \right\} = & \\
 - \frac{\mu}{Re} a_n \int_{\Omega} \left(\xi_{ni} \left(a_k \xi_{ki,j} + a_k \xi_{kji} - \frac{2}{3} a_l \xi_{lh,h} \delta_{ij} \right) \right)_{,j} \eta_r \, d\Omega = & \\
 - \frac{\mu}{Re} \int_{\Omega} \left(\mathbf{u}_i (\mathbf{u}_{i,j} + \mathbf{u}_{j,i} - \frac{2}{3} \mathbf{u}_{h,h} \delta_{ij}) \right)_{,j} \eta_r \, d\Omega. & \quad (45)
 \end{aligned}$$

Therefore, the Galerkin projection expression of the energy equation on arbitrary temperature basis η_r is obtained:

$$\begin{aligned}
 G_r^{pT} = & \frac{1}{(\gamma-1)\gamma Ma^2} c_{m,t} \int_{\Omega} \mathcal{D} \eta_m \eta_r \, d\Omega + \frac{1}{(\gamma-1)\gamma Ma^2} b_{l,t} \int_{\Omega} \zeta_l \mathcal{T} \eta_r \, d\Omega + \frac{1}{2} b_{l,t} \int_{\Omega} \zeta_l \mathbf{u}_h \mathbf{u}_h \eta_r \, d\Omega + \\
 & a_{k,t} \int_{\Omega} \mathcal{D} \xi_{kh} \mathbf{u}_h \eta_r \, d\Omega + \frac{1}{(\gamma-1)Ma^2} \int_{\Omega} (\mathcal{D} \mathcal{T} \mathbf{u}_j)_{,j} \eta_r \, d\Omega + \frac{1}{2} \int_{\Omega} (\mathcal{D} \mathbf{u}_h \mathbf{u}_h \mathbf{u}_j)_{,j} \eta_r \, d\Omega - \\
 & \frac{\kappa}{PrRe(\gamma-1)Ma^2} \int_{\Omega} \mathcal{T}_{,jj} \eta_r \, d\Omega - \frac{\mu}{Re} \int_{\Omega} \left[\mathbf{u}_i \left(\mathbf{u}_{i,j} + \mathbf{u}_{j,i} - \frac{2}{3} \mathbf{u}_{h,h} \delta_{ij} \right) \right]_{,j} \eta_r \, d\Omega. & \quad (46)
 \end{aligned}$$

To summarize, the Galerkin projection equations of the following compressible Navier-Stokes equations are obtained:

$$\left\{ \begin{aligned}
 G_r^{pp} &= b_{r,t} + \int_{\Omega} \mathcal{D}\mathbf{u}_{j,j}\zeta_r \, d\Omega + \int_{\Omega} \mathcal{D}_j\mathbf{u}_j\zeta_r \, d\Omega, \\
 G_r^{pu} &= a_{k,t} \int_{\Omega} \mathcal{D}\xi_{ki}\xi_{ri} \, d\Omega + b_{l,t} \int_{\Omega} \zeta_l\mathbf{u}_i\xi_{ri} \, d\Omega + \\
 &\quad \int_{\Omega} (\mathcal{D}\mathbf{u}_i\mathbf{u}_j)_{,j}\xi_{ri} \, d\Omega + \frac{1}{\gamma Ma^2} \int_{\Omega} (\mathcal{D}\mathcal{T}\delta_{ij})_{,j}\xi_{ri} \, d\Omega - \\
 &\quad \frac{\mu}{Re} \int_{\Omega} \left(\mathbf{u}_{i,j} + \mathbf{u}_{j,i} - \frac{2}{3}\mathbf{u}_{h,h}\delta_{ij} \right)_{,j} \xi_{ri} \, d\Omega, \\
 G_r^{pT} &= \frac{1}{(\gamma-1)\gamma Ma^2} c_{m,t} \int_{\Omega} \mathcal{D}\eta_m\eta_r \, d\Omega + \frac{1}{(\gamma-1)\gamma Ma^2} b_{l,t} \int_{\Omega} \zeta_l\mathcal{T}\eta_r \, d\Omega + \frac{1}{2}b_{l,t} \int_{\Omega} \zeta_l\mathbf{u}_h\mathbf{u}_h\eta_r \, d\Omega + \\
 &\quad a_{k,t} \int_{\Omega} \mathcal{D}\xi_{kh}\mathbf{u}_h\eta_r \, d\Omega + \frac{1}{(\gamma-1)Ma^2} \int_{\Omega} (\mathcal{D}\mathcal{T}\mathbf{u}_j)_{,j}\eta_r \, d\Omega + \frac{1}{2} \int_{\Omega} (\mathcal{D}\mathbf{u}_h\mathbf{u}_h\mathbf{u}_j)_{,j}\eta_r \, d\Omega - \\
 &\quad \frac{\kappa}{PrRe(\gamma-1)Ma^2} \int_{\Omega} \mathcal{T}_{,jj}\eta_r \, d\Omega - \frac{\mu}{Re} \int_{\Omega} \left[\mathbf{u}_i \left(\mathbf{u}_{i,j} + \mathbf{u}_{j,i} - \frac{2}{3}\mathbf{u}_{h,h}\delta_{ij} \right) \right]_{,j} \eta_r \, d\Omega.
 \end{aligned} \right. \tag{47}$$

Therefore, one obtains

$$\left\{ \begin{aligned}
 b_{r,t} + \int_{\Omega} \mathcal{D}\mathbf{u}_{j,j}\zeta_r \, d\Omega + \int_{\Omega} \mathcal{D}_j\mathbf{u}_j\zeta_r \, d\Omega &= 0, \\
 a_{k,t} \int_{\Omega} \mathcal{D}\xi_{ki}\xi_{ri} \, d\Omega + b_{l,t} \int_{\Omega} \zeta_l\mathbf{u}_i\xi_{ri} \, d\Omega + \int_{\Omega} \mathcal{D}_j\mathbf{u}_i\mathbf{u}_j\xi_{ri} \, d\Omega + \\
 &\quad \int_{\Omega} \mathcal{D}\mathbf{u}_{i,j}\mathbf{u}_j\xi_{ri} \, d\Omega + \int_{\Omega} \mathcal{D}\mathbf{u}_i\mathbf{u}_{j,j}\xi_{ri} \, d\Omega + \\
 &\quad \frac{1}{\gamma Ma^2} \int_{\Omega} \mathcal{D}_j\mathcal{T}\xi_{rj} \, d\Omega + \frac{1}{\gamma Ma^2} \int_{\Omega} \mathcal{D}\mathcal{T}_{,j}\xi_{rj} \, d\Omega - \\
 &\quad \frac{\mu}{Re} \int_{\Omega} \left(\mathbf{u}_{i,jj} + \mathbf{u}_{j,ij} - \frac{2}{3}\mathbf{u}_{h,hi} \right) \xi_{ri} \, d\Omega = 0, \\
 \frac{1}{(\gamma-1)\gamma Ma^2} c_{m,t} \int_{\Omega} \mathcal{D}\eta_m\eta_r \, d\Omega + \frac{1}{(\gamma-1)\gamma Ma^2} b_{l,t} \int_{\Omega} \zeta_l\mathcal{T}\eta_r \, d\Omega + \frac{1}{2}b_{l,t} \int_{\Omega} \zeta_l\mathbf{u}_h\mathbf{u}_h\eta_r \, d\Omega + \\
 &\quad a_{k,t} \int_{\Omega} \mathcal{D}\xi_{kh}\mathbf{u}_h\eta_r \, d\Omega + \frac{1}{(\gamma-1)Ma^2} \int_{\Omega} \mathcal{D}_j\mathcal{T}\mathbf{u}_j\eta_r \, d\Omega + \frac{1}{(\gamma-1)Ma^2} \int_{\Omega} \mathcal{D}\mathcal{T}_{,j}\mathbf{u}_j\eta_r \, d\Omega + \\
 &\quad \frac{1}{(\gamma-1)Ma^2} \int_{\Omega} \mathcal{D}\mathcal{T}\mathbf{u}_{j,j}\eta_r \, d\Omega + \frac{1}{2} \int_{\Omega} \mathcal{D}_j\mathbf{u}_h\mathbf{u}_h\mathbf{u}_j\eta_r \, d\Omega + \int_{\Omega} \mathcal{D}\mathbf{u}_{h,j}\mathbf{u}_h\mathbf{u}_j\eta_r \, d\Omega + \\
 &\quad \frac{1}{2} \int_{\Omega} \mathcal{D}\mathbf{u}_h\mathbf{u}_h\mathbf{u}_{j,j}\eta_r \, d\Omega - \frac{\kappa}{PrRe(\gamma-1)Ma^2} \int_{\Omega} \mathcal{T}_{,jj}\eta_r \, d\Omega - \\
 &\quad \frac{\mu}{Re} \int_{\Omega} \left(\mathbf{u}_{i,j}\mathbf{u}_{i,j} + \mathbf{u}_{i,j}\mathbf{u}_{j,i} - \frac{2}{3}\mathbf{u}_{j,j}\mathbf{u}_{h,h} \right) \eta_r \, d\Omega - \\
 &\quad \frac{\mu}{Re} \int_{\Omega} \left(\mathbf{u}_i\mathbf{u}_{i,jj} + \mathbf{u}_i\mathbf{u}_{j,ij} - \frac{2}{3}\mathbf{u}_i\mathbf{u}_{h,hi} \right) \eta_r \, d\Omega = 0.
 \end{aligned} \right. \tag{48}$$

From this one obtains SCOLDDS equations eq. (49) for compressible Navier-Stokes equations:

$$\left\{ \begin{aligned}
 b_{r,t} &= \mathcal{A}_r^I, \\
 a_{k,t}\mathcal{B}_{kr}^I + b_{l,t}\mathcal{B}_{lr}^{II} &= \mathcal{B}_r^{III}, \\
 c_{m,t}\mathcal{C}_{mr}^I + b_{l,t}\mathcal{C}_{lr}^{II} + a_{k,t}\mathcal{C}_{kr}^{III} &= \mathcal{C}_r^{IV},
 \end{aligned} \right. \tag{49}$$

where the coefficients are shown in eq. (51). The initial conditions are as follow:

$$\begin{cases} b_k(0) = (\rho(0), \zeta_k), \\ a_k(0) = (u_i(0), \xi_{ki}), \\ c_k(0) = (T(0), \eta_k), \end{cases} \tag{50}$$

$$\begin{cases} \mathcal{A}_r^I = -\left(\int_{\Omega} \mathcal{D}\mathcal{U}_{j,j}\zeta_r \, d\Omega + \int_{\Omega} \mathcal{D}_{,j}\mathcal{U}_j\zeta_r \, d\Omega\right), \\ \mathcal{B}_{kr}^I = \int_{\Omega} \mathcal{D}\xi_{ki}\xi_{ri} \, d\Omega, \\ \mathcal{B}_{lr}^{II} = \int_{\Omega} \zeta_l \mathcal{U}_i \xi_{ri} \, d\Omega, \\ \mathcal{B}_r^{III} = -\left[\int_{\Omega} \mathcal{D}_{,j}\mathcal{U}_i \mathcal{U}_j \xi_{ri} \, d\Omega + \int_{\Omega} \mathcal{D}\mathcal{U}_{i,j}\mathcal{U}_j \xi_{ri} \, d\Omega + \int_{\Omega} \mathcal{D}\mathcal{U}_i \mathcal{U}_{j,j} \xi_{ri} \, d\Omega + \right. \\ \left. \frac{1}{\gamma Ma^2} \left(\int_{\Omega} \mathcal{D}_{,j}\mathcal{T} \xi_{rj} \, d\Omega + \int_{\Omega} \mathcal{D}\mathcal{T}_{,j} \xi_{rj} \, d\Omega\right) - \frac{\mu}{Re} \int_{\Omega} \left(\mathcal{U}_{i,jj} + \mathcal{U}_{j,ij} - \frac{2}{3}\mathcal{U}_{h,hi}\right) \xi_{ri} \, d\Omega\right], \\ C_{mr}^I = \frac{1}{(\gamma-1)\gamma Ma^2} \int_{\Omega} \mathcal{D}\eta_m \eta_r \, d\Omega, \\ C_{lr}^{II} = \frac{1}{(\gamma-1)\gamma Ma^2} \int_{\Omega} \zeta_l \mathcal{T} \eta_r \, d\Omega + \frac{1}{2} \int_{\Omega} \zeta_l \mathcal{U}_h \mathcal{U}_h \eta_r \, d\Omega, \\ C_{kr}^{III} = \int_{\Omega} \mathcal{D}\xi_{kh} \mathcal{U}_h \eta_r \, d\Omega, \\ C_r^{IV} = -\left\{\frac{1}{(\gamma-1)Ma^2} \left(\int_{\Omega} \mathcal{D}_{,j}\mathcal{T} \mathcal{U}_{j\eta_r} \, d\Omega + \int_{\Omega} \mathcal{D}\mathcal{T}_{,j} \mathcal{U}_{j\eta_r} \, d\Omega + \int_{\Omega} \mathcal{D}\mathcal{T} \mathcal{U}_{j,j} \eta_r \, d\Omega\right) + \right. \\ \left. \int_{\Omega} \mathcal{D}\mathcal{U}_{h,j} \mathcal{U}_h \mathcal{U}_{j\eta_r} \, d\Omega + \frac{1}{2} \left(\int_{\Omega} \mathcal{D}_{,j}\mathcal{U}_h \mathcal{U}_h \mathcal{U}_{j\eta_r} \, d\Omega + \int_{\Omega} \mathcal{D}\mathcal{U}_h \mathcal{U}_h \mathcal{U}_{j,j} \eta_r \, d\Omega\right) - \right. \\ \left. \frac{\kappa}{PrRe(\gamma-1)Ma^2} \int_{\Omega} \mathcal{T}_{,jj} \eta_r \, d\Omega - \frac{\mu}{Re} \left[\int_{\Omega} \left(\mathcal{U}_{i,j} \mathcal{U}_{i,j} + \mathcal{U}_{i,j} \mathcal{U}_{j,i} - \frac{2}{3}\mathcal{U}_{j,j} \mathcal{U}_{h,h}\right) \eta_r \, d\Omega + \right. \right. \\ \left. \left. \int_{\Omega} \left(\mathcal{U}_i \mathcal{U}_{i,jj} + \mathcal{U}_i \mathcal{U}_{j,ij} - \frac{2}{3}\mathcal{U}_i \mathcal{U}_{h,hi}\right) \eta_r \, d\Omega\right]\right\}. \end{cases} \tag{51}$$

4.2.2 The Numerical Realization of Boundary Conditions

Two methods are used to satisfy the boundary conditions, simultaneously, i.e.:

1) The optimal bases satisfying the boundary conditions are obtained with the optimal control method.

2) Boundary conditions $\mathcal{F}_{\partial\Omega}$ are further satisfied in the physical space in solution of the dynamical system equations. Next, the boundary conditions of velocity \mathbf{u} are taken as an example.

① Free-slip boundary conditions

$$\begin{cases} (a_k \xi_{ki} n_i)^{bd} = 0, \\ (a_k \xi_{ki} s_i)^{bd} = a_k (\xi_{ki} s_i)_{\partial\Omega^-}, \\ (a_k \xi_{ki} t_i)^{bd} = a_k (\xi_{ki} t_i)_{\partial\Omega^-}, \end{cases} \tag{52}$$

where superscript “bd” represents the boundary mesh, and subscript $\partial\Omega^-$ represents a layer of mesh near the boundary.

② Nonslip boundary conditions

$$(a_k \xi_{ki})^{bd} = 0. \tag{53}$$

③ Inflow boundary conditions

$$(a_k \xi_{ki})^{bd} = u_{bi}, \tag{54}$$

where u_{bi} is the inlet velocity distribution function.

④ Continuous outflow boundary condition

$$(a_k \xi_{ki})^{bd} = a_k (\xi_{ki})_{\partial\Omega^-}. \tag{55}$$

⑤ Periodic boundary conditions

$$\begin{cases} (a_k \xi_{ki})^{\text{bd}} = a_k(\xi_{ki})_{\partial\Omega^-}, \\ (a_k \xi_{ki})^{\widetilde{\text{bd}}} = a_k(\xi_{ki})_{\partial\Omega^+}, \end{cases} \quad (56)$$

where superscripts “bd” and “ $\widetilde{\text{bd}}$ ” represent a pair of periodic boundaries, and subscripts $\partial\Omega^-$ and $\partial\Omega^+$ represent layers of mesh close to a pair of periodic boundaries, respectively.

⑥ For the compressible Navier-Stokes equations, the density boundary condition and the temperature boundary condition should also be satisfied. Specific methods for temperature and density are similar to the relevant parts of the above velocity boundary conditions and will not be repeated here.

4.3 The Optimal Functional of SCOLDDS for Compressible Navier-Stokes Equations

4.3.1 The Optimal Functional that Approximates Initial Condition J and Its Gradient Equation

The optimal objective functional approximating the initial condition is

$$\begin{aligned} J(\xi_{ki}) = & \int_{\Omega} (u_{Ri}(0), u_{Ri}(0)) \, d\Omega + \int_{\Omega} (\rho_R(0), \rho_R(0)) \, d\Omega + \int_{\Omega} (T_R(0), T_R(0)) \, d\Omega = \\ & \int_{\Omega} (u_i(0) - a_k(0)\xi_{ki})(u_i(0) - a_k(0)\xi_{ki}) \, d\Omega + \\ & \int_{\Omega} (\rho(0) - b_k(0)\zeta_k)(\rho(0) - b_k(0)\zeta_k) \, d\Omega + \\ & \int_{\Omega} (T(0) - c_k(0)\eta_k)(T(0) - c_k(0)\eta_k) \, d\Omega = \\ & \int_{\Omega} [u_i(0)u_i(0) - 2a_k(0)\xi_{ki}u_i(0) + a_k(0)\xi_{ki}a_k(0)\xi_{ki}] \, d\Omega + \\ & \int_{\Omega} [\rho(0)\rho(0) - 2b_k(0)\zeta_k\rho(0) + b_k(0)\zeta_k b_k(0)\zeta_k] \, d\Omega + \\ & \int_{\Omega} [T(0)T(0) - 2c_k(0)\eta_k T(0) + c_k(0)\eta_k c_k(0)\eta_k] \, d\Omega, \end{aligned} \quad (57)$$

where $u_i(0), \rho(0), T(0)$ are the known initial values.

The following gradient equation can be obtained by finding the variation in eq. (57) and making the variation zero:

$$\begin{cases} a_k(0)\xi_{ki} - u_i(0) = 0, \\ b_k(0)\zeta_k - \rho(0) = 0, \\ c_k(0)\eta_k - T(0) = 0. \end{cases} \quad (58)$$

The conjugate gradient numerical optimization algorithm (see appendix A) is used to solve eq. (58).

4.3.2 The Multi-Scale Global Optimization Method

Model equation eq. (17) of the OLDDS obtained with the variational method is only the local extremum of generalized optimal objective functional eq. (18) in functional space \mathcal{B}_N , but we hope to obtain the global optimal bases in whole space \mathcal{B}_N . However, according to the fundamental theorem of global optimization: in general, one cannot obtain the global optimal solution unless an infinite number of searches are carried out, in practical calculations, the final convergence result depends on the selection of iterative initial basis (hereinafter referred to as initial bases) $\xi_k^{(0)}$. If $\xi_k^{(0)}$ is near the global minimum of J^s , the final convergence results are the global optimal bases; otherwise, it can only converge to the local extreme point or even a saddle point of J^s .

Here, a multi-scale global optimization method is proposed to find the approximate global optimal solution. Based on the idea of coarse graining, the global optimal value is quickly located by smoothing the local extreme points. Suppose that value distribution J^s of the generalized optimal objective functional corresponding to the exact solution to eq. (2) in space \mathcal{B}_N is shown as the red curve in fig. 2. Then, to find global optimal value A , the following process of the double-scale global optimization method can be implemented, as follows.

1) Coarse graining: a coarse numerical scheme or grid is used to numerically simulate the equation, a set of coarse databases is obtained. The change in generalized optimal objective functional J^{s*} based on the coarse database in space \mathcal{B}_N is shown by the green curve in fig. 2. Coarsening makes the local extremum smooth and it can

be regarded as a convex domain.

2) POD analysis: POD bases are extracted from the coarse database, and since POD bases are optimal for the database, the POD basis is located at point B in fig. 2.

3) Multi-scale computing: the POD basis extracted in step 2) is processed by interpolation to obtain a set of precise bases. Let the blue curve in fig. 2 represent the value of J^{g**} of the generalized optimal functional in space \mathcal{B}_N calculated in the fine grids. Then, the precise bases are located at point C in fig. 2.

4) Numerical optimization: with the precise bases obtained in step 3) as initial basis $\xi_k^{(0)}$, the numerical optimization is carried out by substituting it into OLDDS model eq. (17), final convergence result ξ_k^* is located at point D in fig. 2, and then, ξ_k^* can be considered as the approximate global optimal basis.

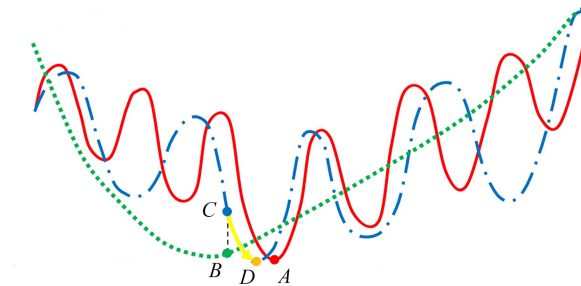


Fig. 2 Schematic diagram of the double-scale global optimization method

According to the idea of double-scale global optimization, it can also be extended to additional multiple scales to obtain more accurate results. It should be emphasized that although the coarse database is used in this method, the database is only used to extract initial basis $\xi_k^{(0)}$, and no longer used in the following optimization process.

4.4 The Solution Procedure

N random bases or POD bases of velocity, density and temperature can be used as the 1st, 2nd and 3rd initial iteration bases of $\xi_{ki}^0, \zeta_k^0, \eta_k^0$, respectively.

1) Initialization:

(a) When the random bases are used as the initial iteration bases, the random number generator is used to generate the initial iteration random bases. When the POD bases are used as the initial iteration bases, the CFD/LES method is used to calculate the flow field of the 1st 500 CFD/LES time steps (Δt), and each flow field is taken for every 10 CFD/LES time steps, then, 50 time sections of the flow field are obtained. From these 50 flow field data, 50 POD bases are obtained with the snapshot POD method, and the 1st N POD bases ($\xi_{ki}^0, \zeta_k^0, \eta_k^0, k = 1 \sim N$) are taken as the initial iteration bases.

(b) With the optimization method which approximates the initial conditions in section 4.3, $\xi_{ki}^*(t, x_i)$, $\zeta_k^*(t, x_i)$ and $\eta_k^*(t, x_i)$ are obtained, and they are orthogonalized and normalized with the Grand-Schmidt method^[36]. Set $t = 0$.

2) Let $t = t + M\Delta t$, where M is the number of intervals of CFD/LES time steps.

3) Use the CFD/LES method to obtain the initial field of the dynamical system used in eq. (57) at $t = t + M\Delta t$.

4) With the initial iteration bases and the optimization method which approximates the initial conditions in section 4.3, $\xi_{ki}^*(t, x_i)$, $\zeta_k^*(t, x_i)$ and $\eta_k^*(t, x_i)$ are obtained, and they are orthogonalized and normalized with the Grand-Schmidt method^[36].

5) By application of the initial conditions, eq. (50) is used to solve the SCOLDDS eq. (49) to obtain $a_k(t)$, $b_k(t)$ and $c_k(t)$. The boundary conditions must be satisfied in the 4 steps of the 4th-order Runge-Kutta method, and the ill-conditioned equation AFD method is used to preprocess the coupled equations.

6) Calculation of the physical quantities of the compressible flow field:

$$\begin{cases} u_i(t, x_i) = a_k(t)\xi_{ki}^*(t, x_i), \\ \rho(t, x_i) = b_k(t)\zeta_k^*(t, x_i), \\ T(t, x_i) = c_k(t)\eta_k^*(t, x_i). \end{cases}$$

7) Return to step 2) until the calculation is completed.

5 Applications of the Construction Theory of SCOLDDS for Compressible Navier-Stokes Equations

In this section, since the flow fields of SCOLDDS and of compressible Navier-Stokes equations are very similar to each other, to save space the legends of flow field nephograms are not shown.

5.1 Definitions of Relative Errors of Flow Field Variables and Proportions of Each Order in the Whole Field

① Relative errors of flow variables in the whole field

In the quantitative comparison of SCOLDDS models with CFD results, the following definition of relative errors of flow variables is used in the whole field, with the relative error of velocity δ_r^u as an example:

$$\delta_r^u = \frac{\int_{\Omega} [(\bar{u} - u)^2 + (\bar{v} - v)^2 + (\bar{w} - w)^2] d\Omega}{\int_{\Omega} [\bar{u}^2 + \bar{v}^2 + \bar{w}^2] d\Omega} \times 100\%, \quad (59)$$

where $\bar{u}, \bar{v}, \bar{w}$ and u, v, w are the results of CFD and SCOLDDS, respectively.

② Proportions of flow variables of each order in the whole field

In order to understand the contribution of each order of flow variables to the total flow of the SCOLDDS, eq. (60) is used to calculate their proportions, as is shown below. Take velocity proportion P_k^u as an example:

$$P_k^u = \frac{\int_{\Omega} (|u_k| + |v_k| + |w_k|) d\Omega}{\int_{\Omega} (|u| + |v| + |w|) d\Omega} \times 100\%, \quad (60)$$

where $|u_k|, |v_k|, |w_k|$ are the absolute values of each component of the velocity field (such as $|u_k| = |a_k \xi_k|$, k does not sum up), and $|u|, |v|, |w|$ are the absolute values of the velocity field (such as $|u| = |a_k \xi_k|$), obtained with the SCOLDDS method, respectively.

5.2 The 3D Compressible Laminar Backward-Facing Step Flow

With this example, we will try to find the answers to following questions:

① How can the solutions to low-dimensional dynamical systems be quantitatively comparable with CFD results?

② What is the accuracy of the quantitative comparison between the results of SCOLDDS and CFD?

③ What is the spatiotemporal evolution of SCOBs with the development of the flow field?

5.2.1 Research Problem

The dimensionless parameters of the 3D compressible laminar backward-facing step flow (fig. 3) are $Re = \frac{\rho_0 \times h \times u_0}{\mu} = 1120$, $Ma = 0.74833148$, $Pr = 0.72$. The finite volume method is used to solve the 3D unsteady compressible Navier-Stokes equations. Orthogonal meshes with equal spacings are used, $M_x \times M_y \times M_z = 85 \times 41 \times 41$, $(\Delta x, \Delta y, \Delta z) = (2.0, 1.0, 1.0)$ m, $\Delta t = 0.1$ s.

The lower part of the left boundary is a nonslip backward-facing step, the upper part of the left boundary is an inflow boundary, the right boundary is a continuous outflow boundary, and the surrounding are nonslip solid wall boundaries. The height of the backward-facing step is $h = 20$ m. The inflow velocity and density at the backward-facing step of the left boundary are $\mathbf{u}_0 = (u_0, v_0, w_0) = (0.56, 0.0, 0.0)$ m/s and $\rho_0 = 1.0$ kg/m³, respectively, $\mu = 0.01$ Pa·s.

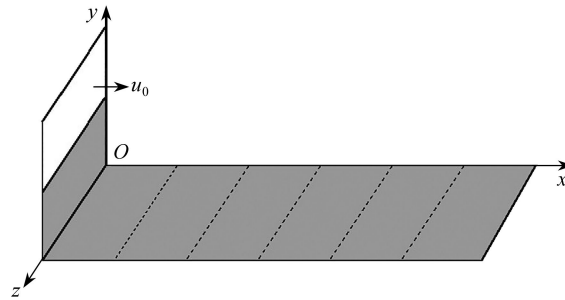


Fig. 3 The 3D sketch map of the compressible laminar backward-facing step flow

The SCOBs with truncation $N = 3$ are used to construct the SCOLDDS model for compressible Navier-Stokes equations, and their solutions are compared with CFD results quantitatively in real time.

5.2.2 Numerical Experiments Predictability on the Low-Dimensional Dynamical System Models

In order to understand why the SCOBs are the key to obtaining the SCOLDDS, which ensures that the approximate solution to the SCOLDDS is in the attraction domain of the numerical solution of CFD (and the infinite-dimensional Navier-Stokes equations), a set of numerical experiments is conducted on the predictability of low-dimensional dynamical system models based on spatial bases and SCOBs with 3D compressible laminar backward step flow. In the numerical experiments the velocity errors of various low-dimensional dynamical system models (such as POD bases, POD bases with a time interval, spatial optimal bases, SCOBs with random initial bases or POD initial bases) are shown in [fig. 4](#).

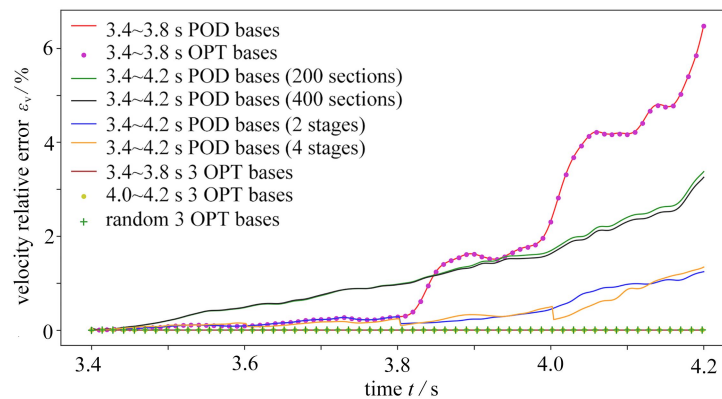


Fig. 4 Comparison of the evolution curves of the velocity errors with time in the whole field of low-dimensional dynamical system models constructed by POD bases, POD bases with a time interval, spatial optimal bases, SCOBs with random initial bases or POD initial bases

In the following numerical experiments, the low-dimensional dynamical system models are constructed with POD bases, POD bases with a time interval, spatial optimal bases, SCOBs with random initial bases or POD initial bases, and the entire field's velocity errors of each approximate flow field are calculated by eq. (59). Four groups of test cases are studied.

1) Low-dimensional dynamical system models based on POD bases and SCOBs obtained in the period of 3.4 ~ 3.8 s

① In the period of 3.4 ~ 3.8 s, 200 snapshot POD bases are constructed, and then, the 1st 30 POD bases are used to obtain the low-dimensional dynamical system model through the Galerkin projection, and the approximate flow field of 3.4 ~ 4.2 s is obtained with the model.

② In the period of 3.4 ~ 3.8 s, the 3rd order spatial optimal bases are constructed; the low-dimensional dynamical system model is obtained through the Galerkin projection, and the approximate flow field of 3.4 ~ 4.2 s is obtained with the model.

2) Low-dimensional dynamical system models based on POD bases and SCOBs obtained in the period of

3.4 ~ 4.2 s

① In the period of 3.4 ~ 4.2 s, 200 snapshot POD bases are constructed; the 1st 30 POD bases are then used to obtain the low-dimensional dynamical system model through the Galerkin projection, and the approximate flow field of 3.4 ~ 4.2 s is obtained with the model.

② In the period of 3.4 ~ 4.2 s, 400 snapshot POD bases are constructed; the 1st 30 POD bases are then used to obtain the low-dimensional dynamical system model through the Galerkin projection, and the approximate flow field of 3.4 ~ 4.2 s is obtained by using the model.

3) Low-dimensional dynamical system models based on POD bases and SCOBs obtained in the multiple short periods

① In the periods of 3.4 ~ 3.8 s and 3.8 ~ 4.2 s, 200 snapshot POD bases are constructed for each period; the 1st 30 POD bases are then used to obtain the low-dimensional dynamical system model through the Galerkin projection for each period, and the approximate flow field of 3.4 ~ 4.2 s is obtained with this 2-time-interval model.

② In the periods of 3.4 ~ 3.6 s, 3.6 ~ 3.8 s, 3.8 ~ 4.0 s and 4.0 ~ 4.2 s, 200 snapshot POD bases are constructed for each period; the 1st 30 POD bases are then used to obtain the low-dimensional dynamical system model through the Galerkin projection for each period, and the approximate flow field of 3.4 ~ 4.2 s is obtained with this 4-time-interval model.

4) Low-dimensional dynamical system models based on SCOBs

① In the period of 3.4 ~ 3.8 s, 3.8 ~ 4.0 s and 4.0 ~ 4.2 s, 3rd-order SCOBs with 3rd-order POD bases as initial bases are constructed.

② Third-order SCOBs with 3rd-order random initial bases are constructed; the low-dimensional dynamical system model is obtained through the Galerkin projection, and the approximate flow field of 3.4 ~ 4.2 s is obtained with these models.

From [fig. 4](#), it can be seen that:

(a) The dynamical system model based on spatial bases (including POD bases and spatial optimal bases) has fewer errors in the period of generating these bases, but the error becomes continually larger in the following time. Therefore, the low-dimensional dynamical system model based on spatial bases (including POD bases and spatial optimal bases) is not predictable.

(b) The error of the low-dimensional dynamical system model built on spatial bases constructed with a set of shorten period of data is smaller than that of with a set of longer period of data.

(c) The low-dimensional dynamical system model built on the SCOBs with random initial bases or POD initial bases can accurately approximate the CFD results, and the interval of solving SCOBs is not limited by the constrains of ergodic condition of each state in the snapshot-POD, and which can be from each CFD time step (dt) to any CFD time steps. At the same time, because the calculation of seeking the SCOBs does not rely on big flow field data, and its optimization convergence is very fast, the SCOLDDS model can be built efficiently and flexibly.

Therefore, one can arrive the conclusion that only with SCOBs, the accurate quantitative comparison between solutions of the SCOLDDS and the CFD of compressible Navier-Stokes equations is possible.

5.2.3 Results of Construction of SCOLDDS for Compressible Navier-Stokes Equations

With 3D Compressible Laminar Backward-Facing Step Flow

① Time evolution curves of errors of compressible SCOLDDS models

It can be seen from [fig. 5](#) that at the beginning, because the initial iteration bases of velocity, density and temperature are the 3rd-order POD bases, the errors of flow field variables are large and then decrease rapidly during the solution SCOBs in the initial short time ($N=3$, $Re=1\ 120$, $Ma=0.748\ 331\ 48$, $Pr=0.72$). Second, the whole field error of the approximate flow field of the compressible SCOLDDS is kept below 0.01%, which shows that the

average error at each point is kept below $0.01\% / (85 \times 41 \times 41) = 7 \times 10^{-8}\%$.

② Time evolution of the flow field: CFD vs. OLDDDS

From fig. 6, one can see the time evolution of the numerical solution with the finite volume method of Navier-Stokes equations and the approximate optimal solution of the 3rd-order SCOLDDDS. The initial error is still obvious even after the optimal optimization because the POD bases are used as the initial iteration bases. However, after several optimal optimization processes, the approximate optimal solution of the 3rd-order SCOLDDDS is very close to the numerical solution of CFD.

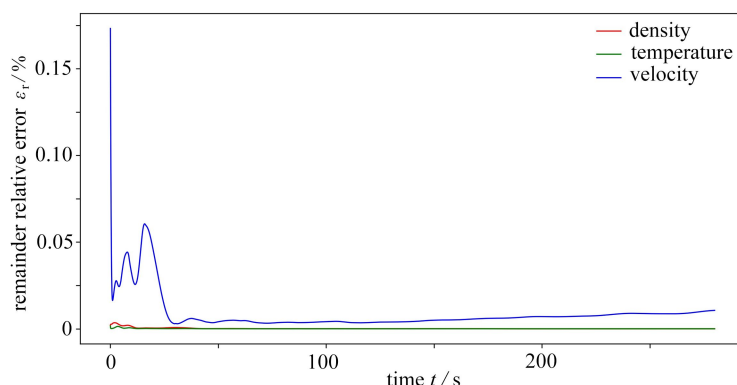


Fig. 5 Time evolution curves of errors of velocity, density and temperature

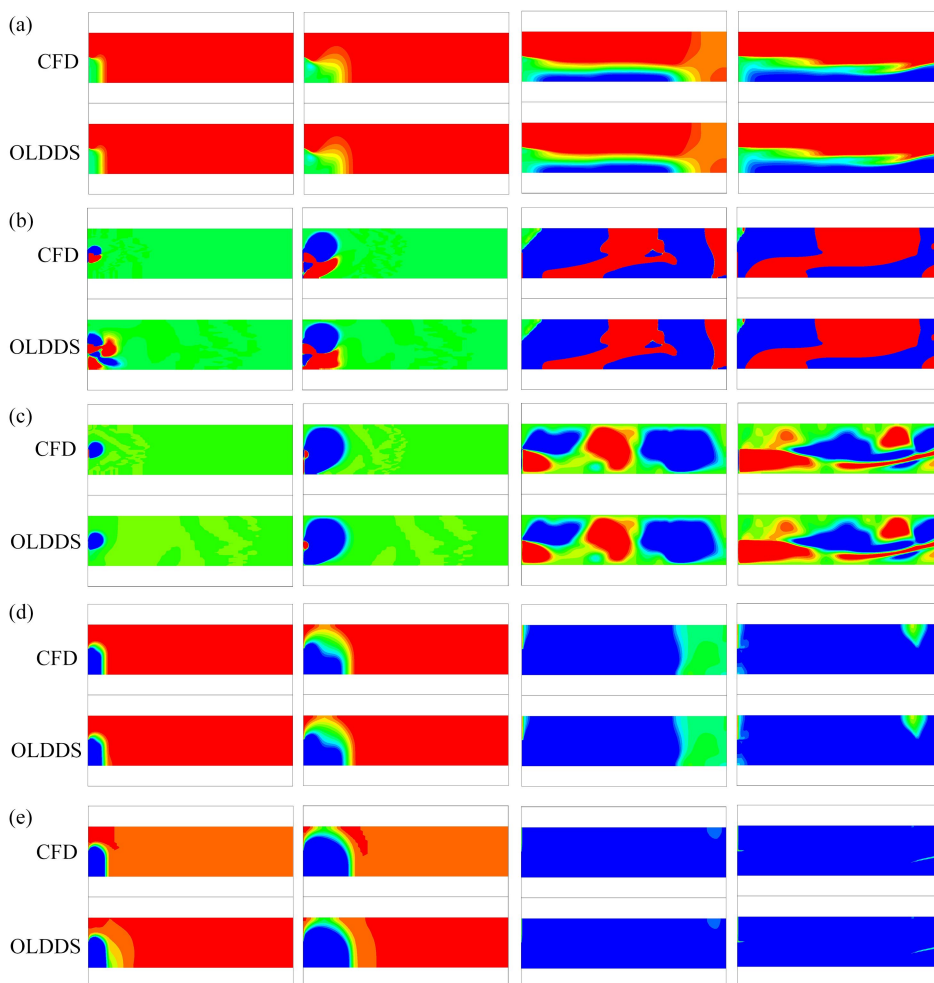


Fig. 6 Comparison of time evolution of flow fields of CFD and OLDDDS, from left to right, $t = 100\text{ s}, 300\text{ s}, 5\ 000\text{ s}, 9\ 990\text{ s}$:
(a) velocity field u ; (b) velocity field v ; (c) velocity field w ; (d) density field ρ ; (e) temperature field T

Therefore, the modelling method of SCOLDDS can obtain a high-precision approximate solution compared with the numerical solution of CFD and ensure that the optimal solution of the SCOLDDS with truncation $N = 3$ is within the attraction domain of the numerical solution of the high-dimensional CFD (and with the infinite-dimensional Navier-Stokes equations). Through analysis of the characteristics of the SCOLDDS with truncation $N = 3$ of the laminar backward-facing step, the exact dynamical system characteristics of the Navier-Stokes equations can be obtained.

③ Time evolution curves of coefficients of SCOBs

It can be seen from fig. 7 that, first, the coefficients of the 1st-order spatiotemporal-coupling velocity optimal basis ξ , density optimal basis ζ and temperature optimal basis η are one-order-magnitude larger than those of the 2nd- and the 3rd-order SCOBs. Therefore, the 1st-order SCOBs are dominant. Second, the coefficients of the 1st-order SCOBs have a lower evolution frequency with time, while the coefficients of the 2nd-order and the 3rd-order SCOBs have higher evolution frequencies with time.

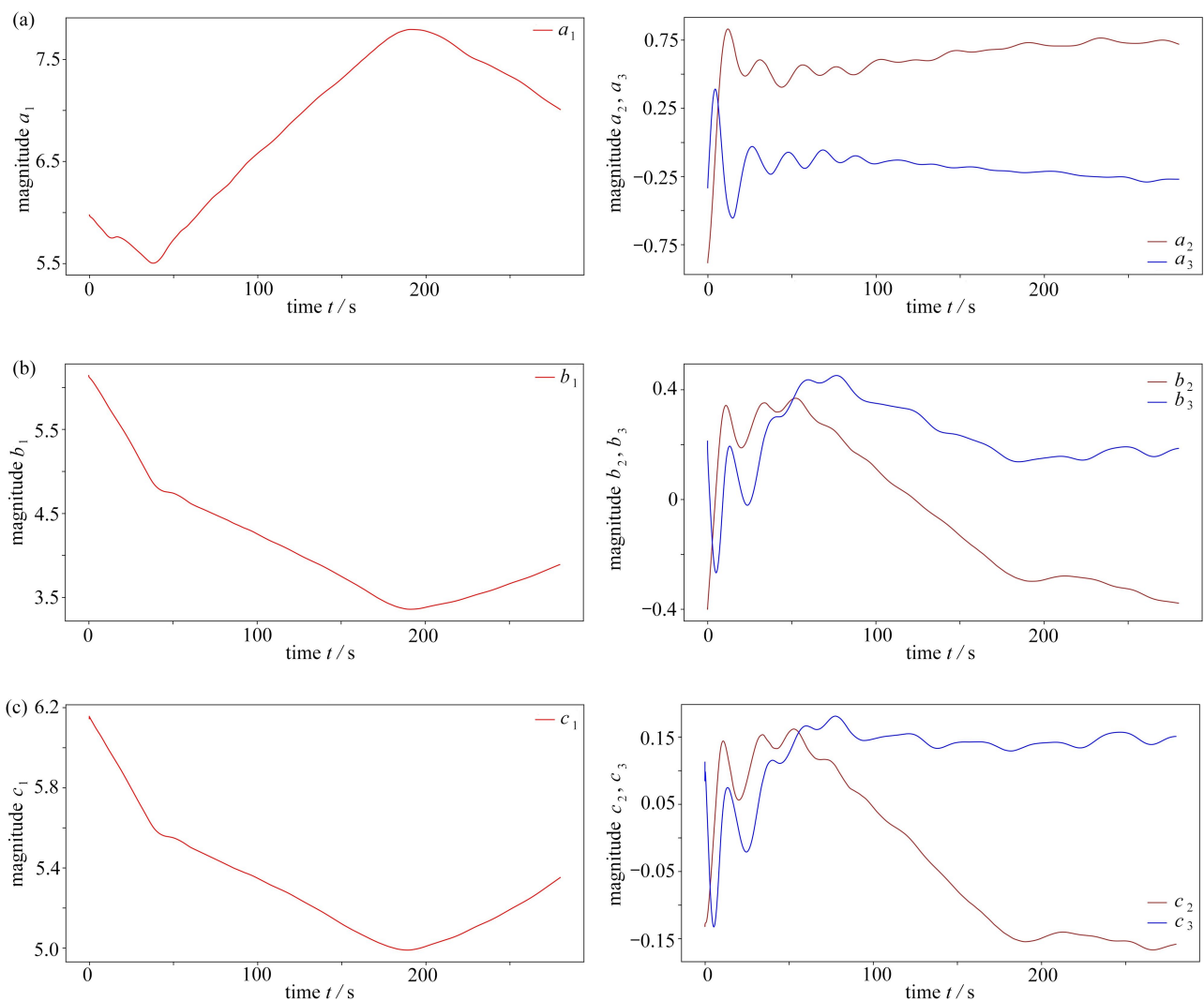


Fig. 7 Time evolution curves of coefficients of velocity basis ξ , density basis ζ and temperature basis η

④ Time evolution of spatiotemporal-coupling optimal velocity basis ξ , density basis ζ and temperature basis η

It can be seen from fig. 8 that, for the laminar backward-facing step flow, the 1st-order spatiotemporal-coupling optimal velocity basis ξ^u , density basis ζ and temperature basis η dominate the time evolution of the flow field, and all evolve with the development of the flow, but their 2nd- and 3rd-order optimal bases basically do not evolve with

time. However, the 1st-, 2nd- and 3rd-order bases of velocity bases ξ^v and ξ^w , which are not dominant in the flow field, have obvious evolution with time. This may be because the 1st-order spatiotemporal-coupling optimal velocity bases ξ^v and ξ^w , which are not dominant in the flow field, have weak control over their 2nd- and 3rd-order SCOBs, the latter 2 can evolve synchronously with the development of the flow.

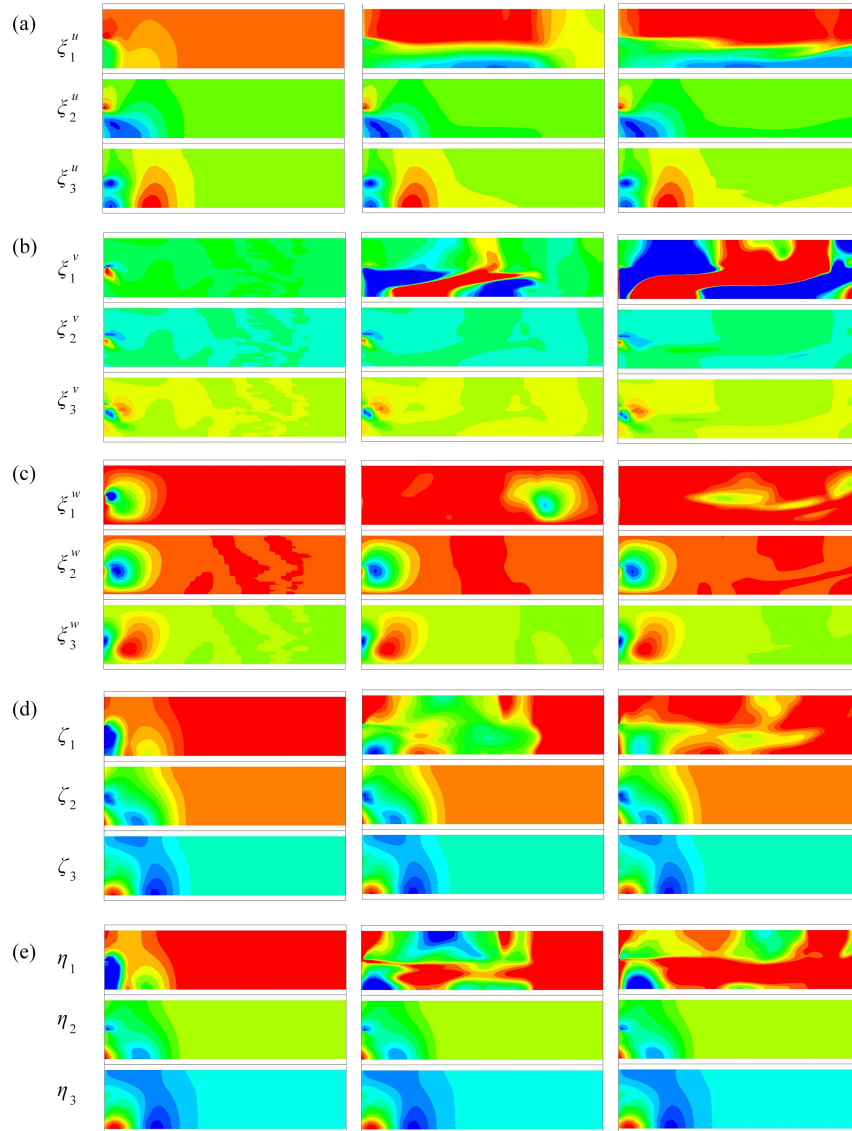


Fig. 8 Time evolution of spatiotemporal-coupling optimal velocity basis ξ , density basis ζ and temperature basis η : from left to right, $t = 100$ s, 5 000 s, 9 990 s

Through the observation of [figs. 7](#) and [8](#), one can draw the following conclusion: it is SCOBs that make SCOLDDS compare with CFD rigorously in numerical solution.

5.3 The 3D Compressible Turbulent Straight Jet

In this example, the answers to following questions will be found:

- ① Can the solutions of low-dimensional dynamical systems of compressible Navier-Stokes equations be quantitatively comparable with those of the large-eddy simulation (LES) of turbulent results?
- ② How is the accuracy of quantitative comparison between the results of SCOLDDS and LES?
- ③ How is the importance of each order of decomposition, i.e., how are the proportions (eq. (60)) of each order of approximate flow variables in the turbulent jet flow with truncation $N = 3$ and 5, respectively?

5.3.1 Research Problem

The dimensionless parameters of the 3D compressible turbulent straight jet flow (fig. 9) are $Re = \frac{\rho_{jet} \times \Phi_{jet} \times u_{jet}}{\mu} = 416\ 081.77$, $Ma = 0.423\ 451\ 80$, $Pr = 0.72$.

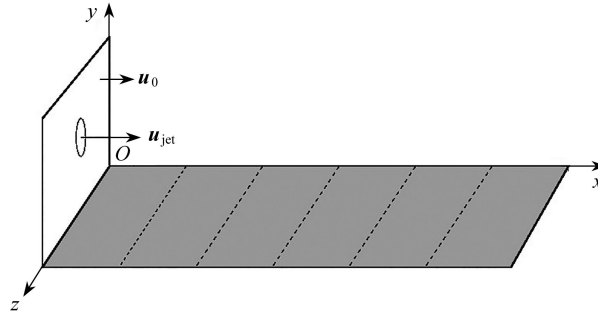


Fig. 9 The 3D sketch map of the compressible turbulent straight jet flow

An LES method^[37] based on the Favre filter^[38-39] and Smagorinsky subgrid model^[40], where Smagorinsky constant $C_s = 0.1$, is used to solve the 3D unsteady compressible LES equations. Orthogonal meshes with equal spacings are used, $M_x \times M_y \times M_z = 105 \times 61 \times 61$, $(\Delta x, \Delta y, \Delta z) = (1.5, 1.0, 1.0)$ m, $\Delta t = 0.000\ 58$ s.

The diameter of the turbulent straight jet at the centre ($y = z = 31$ m) of the yOz plane on the left boundary is $\Phi_{jet} = 6$ m, its inflow velocity is $\mathbf{u}_{jet} = (u_{jet}, v_{jet}, w_{jet}) = (2.0, 0.0, 0.0)$ m/s, and its inflow density is $\rho_{jet} = 0.627\ 59$ kg/m³, $\mu = 0.000\ 018\ 1$ Pa·s. The inflow velocity and inflow density in the non-jet area on the left boundary are $\mathbf{u}_0 = (u_0, v_0, w_0) = (0.3, 0.0, 0.0)$ m/s and $\rho_0 = 1.161\ 03$ kg/m³, respectively, $\mu = 0.000\ 018\ 1$ Pa·s. The right boundary is a continuous outflow boundary, and the surrounding are nonslip solid wall boundaries.

The LES code is combined with the SCOLDDS modelling theory of 3D compressible Navier-Stokes equations to develop a 3D compressible turbulent LES and SCOLDDS modelling toolkit CLOT3D (compressible LES and SCOLDDS tools of 3D compressible Navier-Stokes equations). With this software package, the LES numerical solution of the turbulent straight jet is obtained, which is compared with the SCOLDDS model of compressible Navier-Stokes equations (using SCOBs with truncation $N = 3$ and 5, respectively).

5.3.2 The SCOLDDS of the SCOBs With Truncation $N = 3$

① Time evolution curves of errors of compressible SCOLDDS models

From fig. 10, one can see that, given the turbulent straight jet flow, the time evolution of the velocity error is always very violent, but the whole field error is not large, basically below 0.006%. Since the whole field errors of density and temperature are very small (less than 0.001%), their time evolution process cannot be seen in the figure ($Re=416\ 081.77$, $Ma=0.423\ 451\ 80$, $Pr=0.72$, the same below). Second, because the velocity error of the approximate flow field of the compressible SCOLDDS is kept below 0.006% in the whole field, the average velocity error at each point is kept below $0.006\% / (105 \times 61 \times 61) = 1.5 \times 10^{-8}\%$.

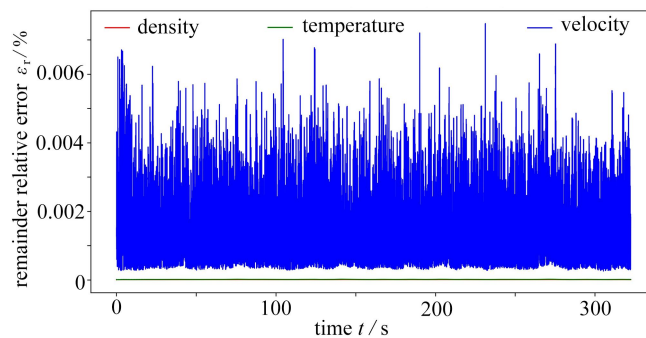


Fig. 10 Time evolution curves of errors of velocity, density and temperature

② Time evolution of the flow field: LES ~ SCOLDDDS

It can be seen from [fig. 11](#) that, for the first time, with the SCOLDDDS model ($N = 3$) for the compressible 3D Navier-Stokes equations can very accurately obtain the numerical results given by the LES method, and from the initial moment, the approximate optimal solution of the SCOLDDDS with truncation $N = 3$ can quickly approach the numerical solution of LES.

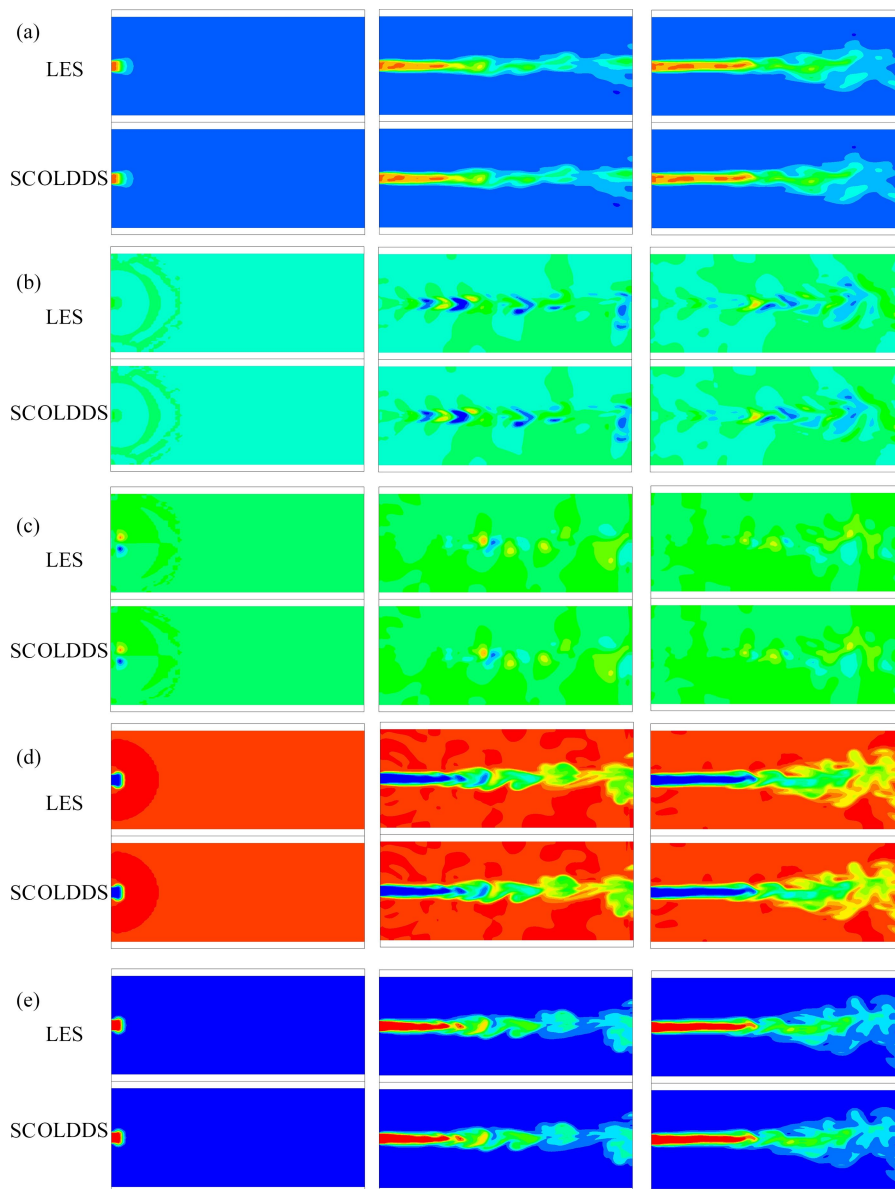


Fig. 11 Comparison of time evolution of turbulent flow fields between the LES and the SCOLDDDS, from left to right, $t = 100 \text{ s}, 5\,000 \text{ s}, 16\,670 \text{ s}$:

(a) velocity field u ; (b) velocity field v ; (c) velocity field w ; (d) density field ρ ; (e) temperature field T

Therefore, a high-precision approximate solution can be obtained with the SCOLDDDS modelling method, which guarantees for the first time that the optimal solution of the SCOLDDDS has the same attraction domain as the numerical solution of the complex turbulent LES. Through analysis of the characteristics of SCOLDDDS of the turbulent straight jet flow, the accurate characteristics of the turbulent dynamical system of the LES equations for the turbulent straight jet flow can be obtained.

③ Time evolution curves of the proportion of each order of approximate flow variables (see eq. (60))

It can be seen from [fig. 12](#) that, the 1st-order velocity field, the density field and the temperature field account

for more than 99.99% of the total flow field, the 2nd- and 3rd-order velocity fields account for less than 0.001 7% of the total flow field, while the 2nd- and 3rd-order density fields and temperature fields account for less than 0.000 1% of the total flow field, respectively. Therefore, the 1st-order SCOBs play very important leading roles, while the 2nd- and 3rd-order SCOBs play auxiliary roles.

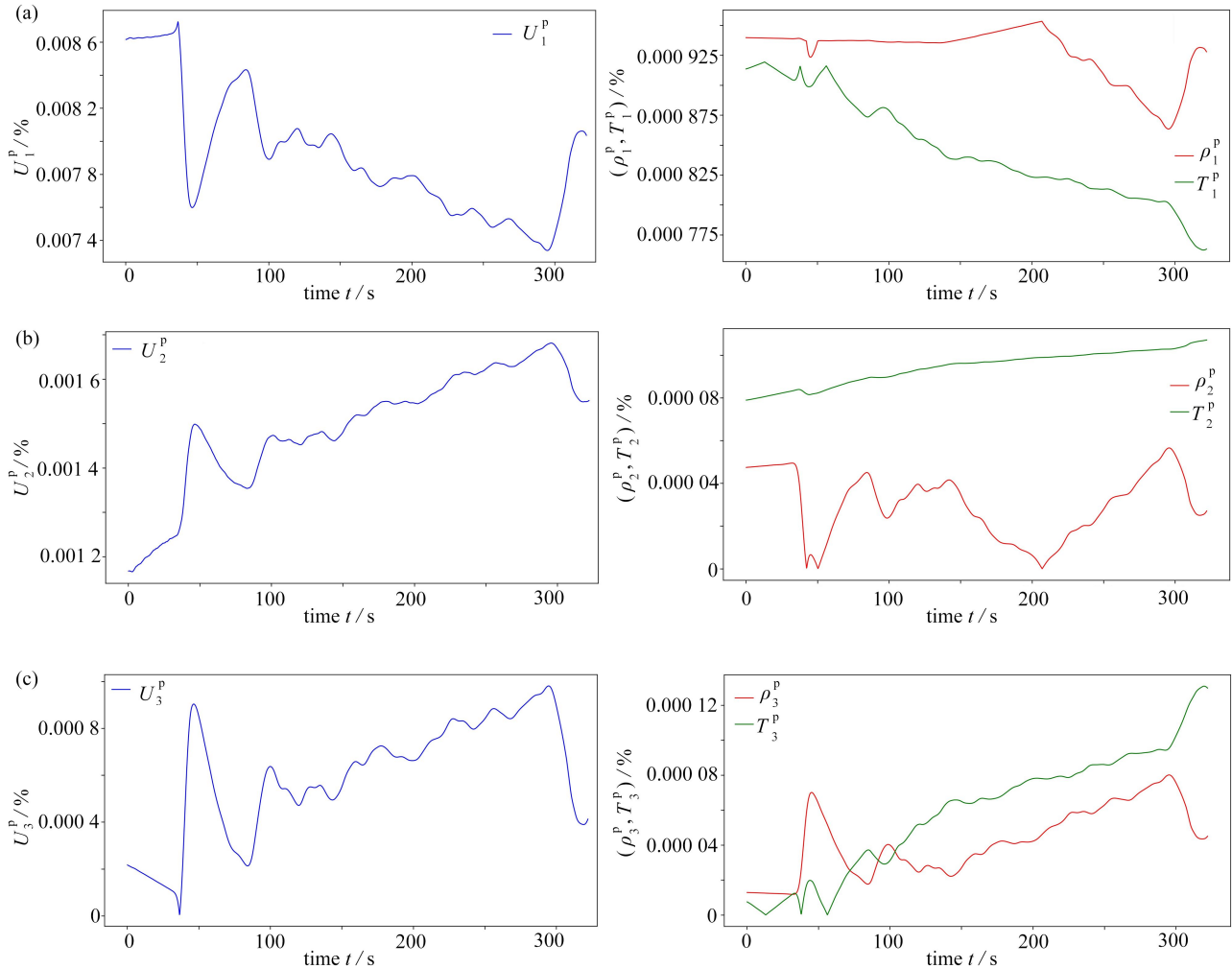


Fig. 12 Time evolution curves of the proportion of each order of approximate flow variables: (a) the 1st-order; (b) the 2nd-order; (c) the 3rd-order

Through the proportion study, one can quantitatively know the accuracy of the approximate optimal solution of the SCOLDDS on the one hand, and on the other hand, one can determine the dimension of the SCOBs through the proportion study of each order of flow fields.

④ Time evolution curves of coefficients of SCOBs

It can be seen from fig. 13 that, the coefficients of the 1st-order spatiotemporal-coupling optimal velocity basis, density basis and temperature basis are 2-orders-magnitude larger than those of the 2nd- and 3rd-order SCOBs; therefore, the 1st-order SCOBs are dominant. Second, even in the turbulent state, the time evolution frequency of the coefficients of the 1st-order SCOBs is still low, while those of the coefficients of the 2nd- and 3rd-order SCOBs are much higher than that in the laminar state, and the 2 are basically the same.

⑤ Time evolution of spatiotemporal-coupling optimal velocity basis ξ , density basis ζ and temperature basis η

It can be seen from fig. 14 that, for the time evolution of the spatiotemporal-coupling optimal velocity basis ξ , density basis ζ and temperature basis η for the turbulent straight jet flow, not only the 1st-order spatiotemporal-coupling optimal velocity basis ξ^u , density basis ζ and temperature basis η evolve into typical turbulent flow patterns

with the development of the flow, but the 2nd- and 3rd-order turbulence structures evolve with time to develop into many small-scale turbulent structures. It is the complex spatiotemporal-coupling evolution of the 2nd- and 3rd-order SCOBs that enable the SCOLDDs to well simulate and analyse turbulent flow.

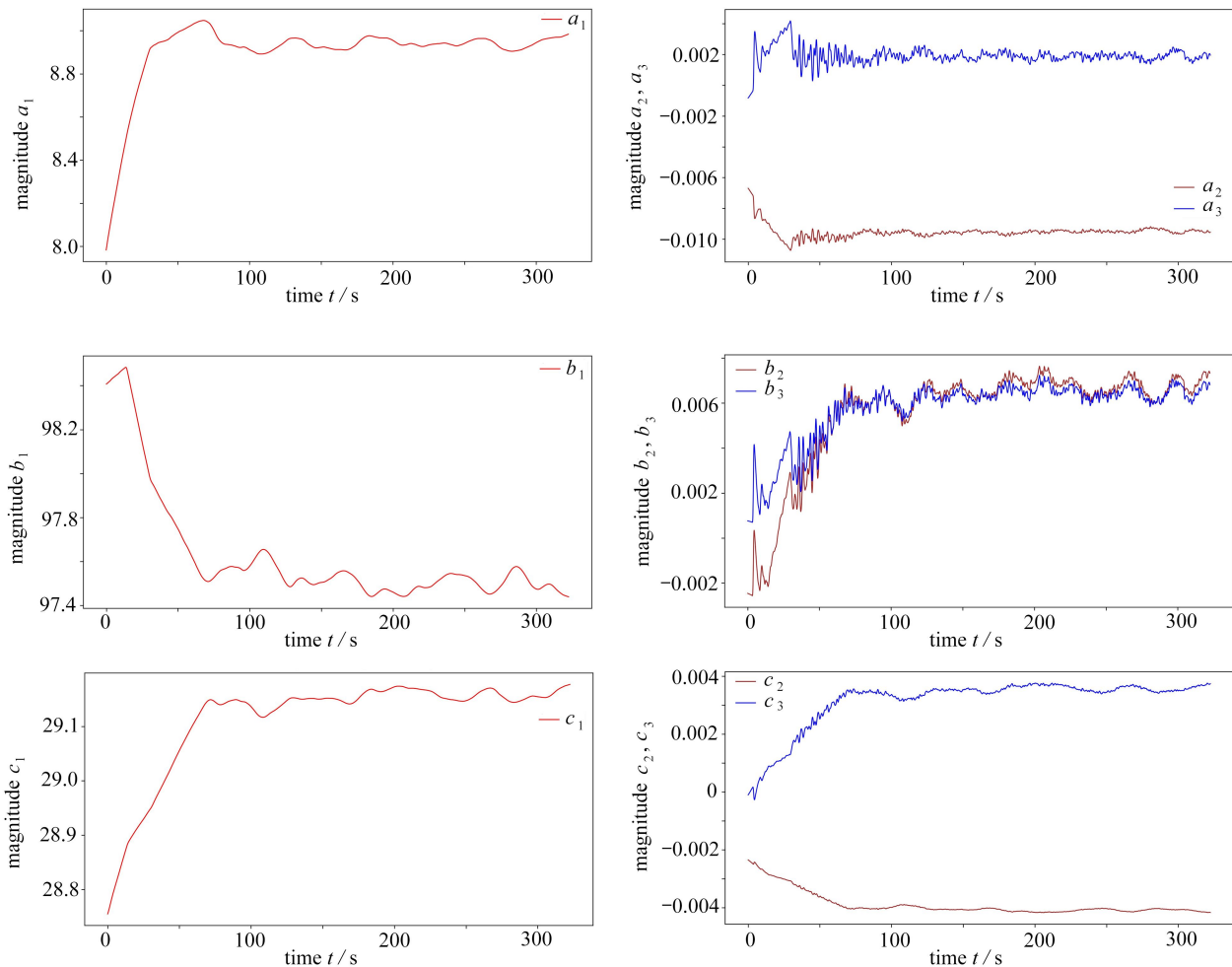


Fig. 13 Time evolution curves of coefficients of velocity basis ξ , density basis ζ and temperature basis η

Through the observation of [figs. 13](#) and [14](#), one can draw the following conclusion: the fundamental reason why the theory of the SCOLDDs can obtain high accuracy and can be comparable to the numerical solution of LES is that, the SCOBs reflecting the characteristics of turbulence pulsation are adopted.

5.3.3 The SCOLDDs of the SCOBs With Truncation $N = 5$

① Time evolution curves of errors of compressible SCOLDDs models

② Time evolution of the flow field: LES \sim OLDDs

Since the results of the SCOBs (OLDDs) with truncation $N = 5$ are almost identical to those with truncation $N = 3$ (see [fig. 11](#)), they are not shown.

Compare [figs. 10](#) and [15](#), one can see that the average global accuracy of the approximate solution of the SCOLDDs (0.002%) with truncation $N = 5$ is higher than that of those with truncation $N = 3$ (0.003%).

③ Time evolution curves of the proportion of each order of approximate flow variables

It can be seen from [figs. 12](#) and [16](#) that, the 1st 3 orders of flow field proportions of the SCOLDDs with truncation $N = 5$ are basically the same as that of the SCOLDDs with truncation $N = 3$, but the evolution laws with time is different. An interesting phenomenon can also be seen from [figs. 12](#) and [16](#) that, from the third-order flow field, the average value of its proportion is approximately half of that of the lower one, that is, the average value of

the proportion between the adjacent higher-order flow fields is an inverse series of 0.5.

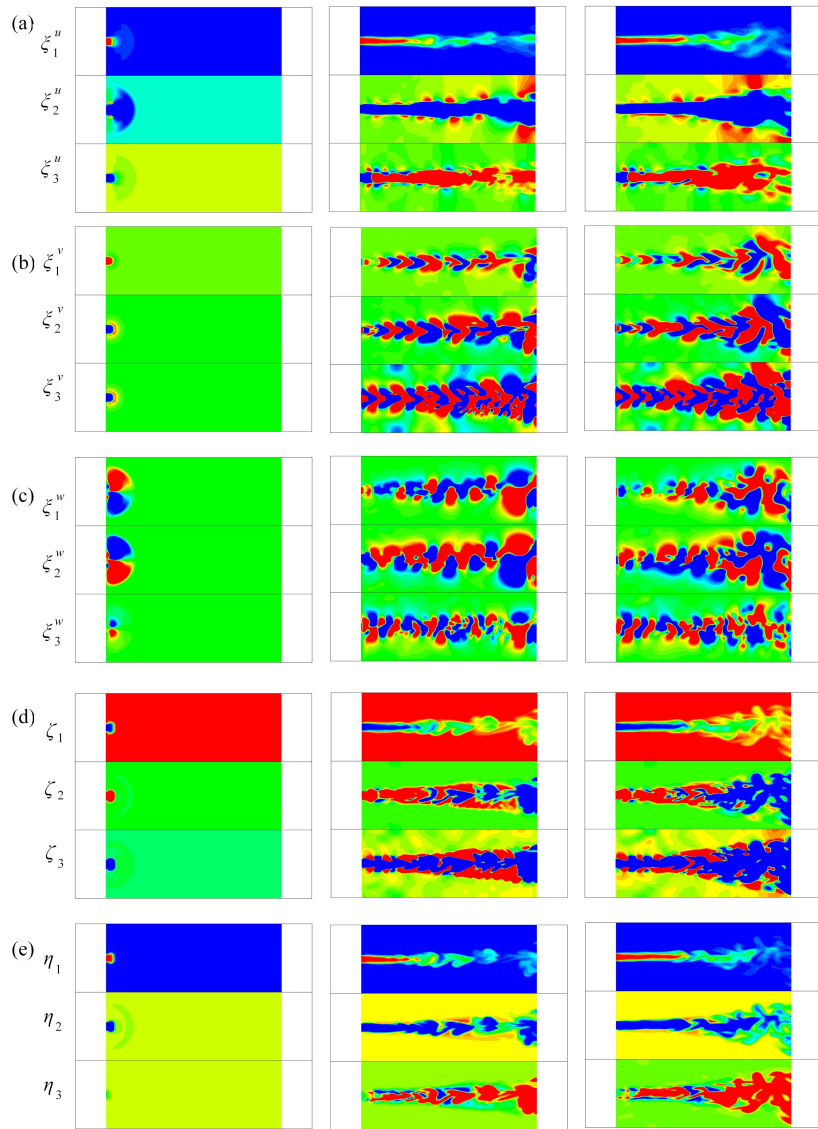


Fig. 14 Time evolution of spatiotemporal-coupling optimal velocity basis ξ , density basis ζ and temperature basis η : from left to right, $t = 100 \text{ s}, 5\,000 \text{ s}, 16\,670 \text{ s}$

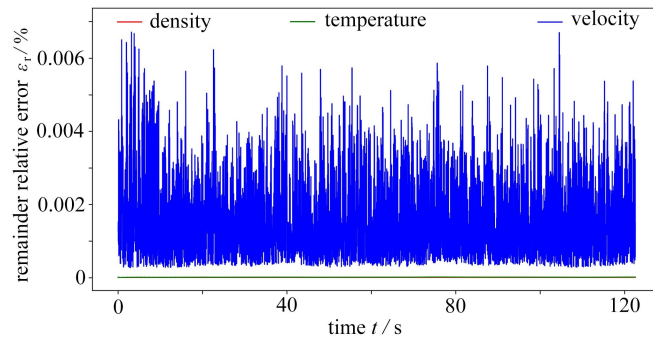


Fig. 15 Time evolution curves of errors of velocity, density and temperature

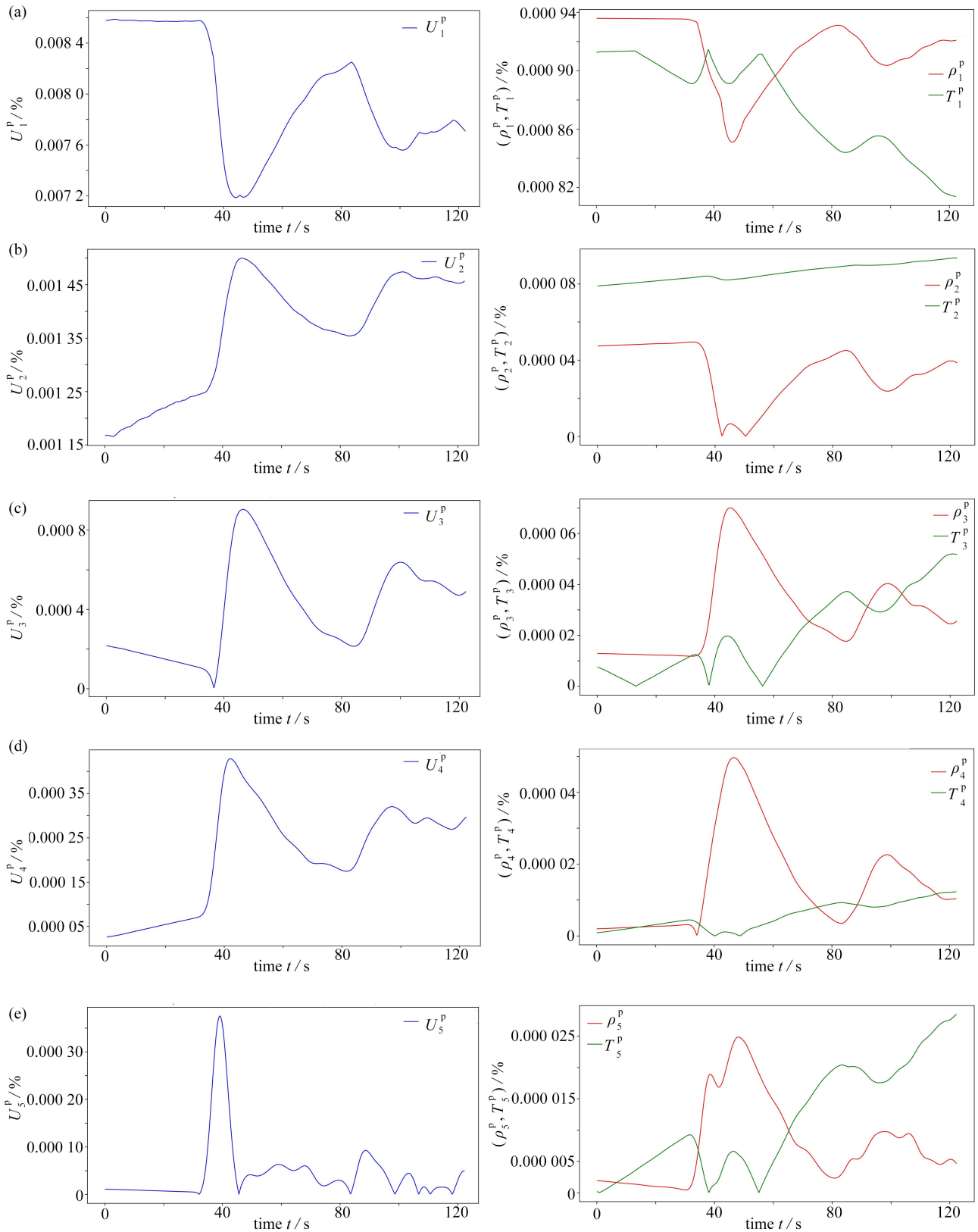


Fig. 16 Time evolution curves of the proportion of each order of approximate flow variables: (a) the 1st order; (b) the 2nd order; (c) the 3rd order; (d) the 4th order; (e) the 5th order

④ Time evolution curves of coefficients of SCOBs

It can be seen from [figs. 13](#) and [17](#) that, first, the coefficient evolution laws of their 1st-order spatiotemporal-

coupling velocity optimal basis ξ , density basis ζ and temperature basis η are basically the same, and they are 2-order-magnitude larger than the coefficients of their 2nd- and 3rd-order SCOBs. Second, for the SCOLDDS with truncation $N = 5$, the coefficients of the 4th-order SCOBs evolve with time with almost the same frequency as the coefficients of the 2nd- and 3rd-order SCOBs, but the coefficients of the 5th-order SCOBs evolve with a time with much higher frequency than those of the previous ones.

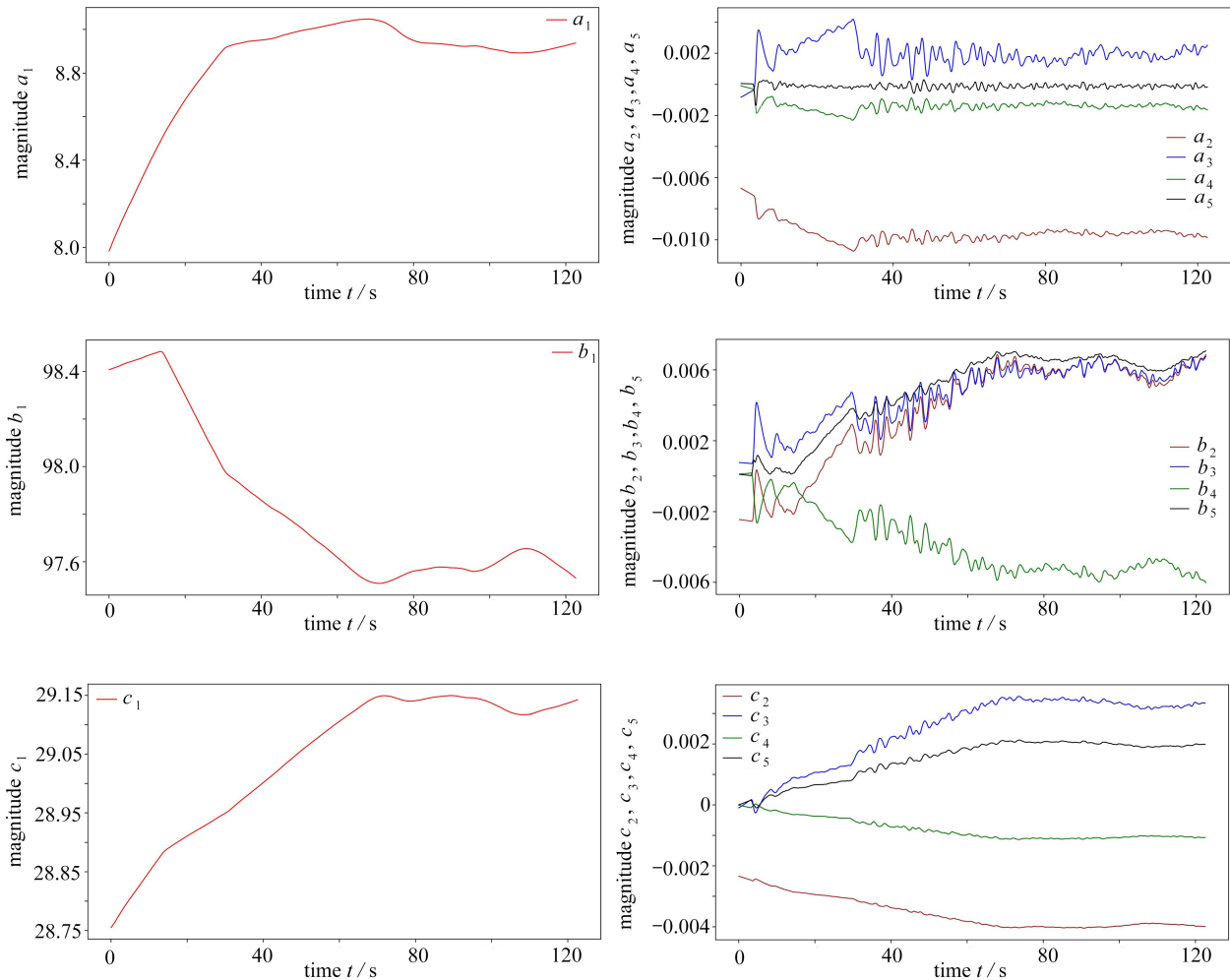


Fig. 17 Time evolution curves of coefficients of velocity basis ξ , density basis ζ and temperature basis η

⑤ Time evolution of spatiotemporal-coupling optimal velocity basis ξ , density basis ζ and temperature basis η

From [figs. 14](#) and [18](#), in the time evolution images of the spatiotemporal-coupling optimal velocity basis ξ , density basis ζ and temperature basis η , for the high-order SCOBs ($N > 1$), odd- and even-order SCOBs pairs are formed, and there are similar evolutions of morphological characteristics between the odd- and even-order SCOBs. However, in the 5th-order SCOBs, there are small-scale spatiotemporal-coupling evolution structures corresponding to high wave numbers.

Through the observation of [figs. 13](#) and [14](#), as well as [figs. 17](#) and [18](#), one can draw the following conclusion: for the compressible turbulent straight jet, the SCOLDDS model with truncation $N = 3$ can compare with CFD solution with high accuracy. If it is necessary to further analyse the spatiotemporal-coupling evolution process and mechanism of turbulent small-scale structures, the SCOLDDS model with truncation $N = 5$ with higher accuracy can be used.

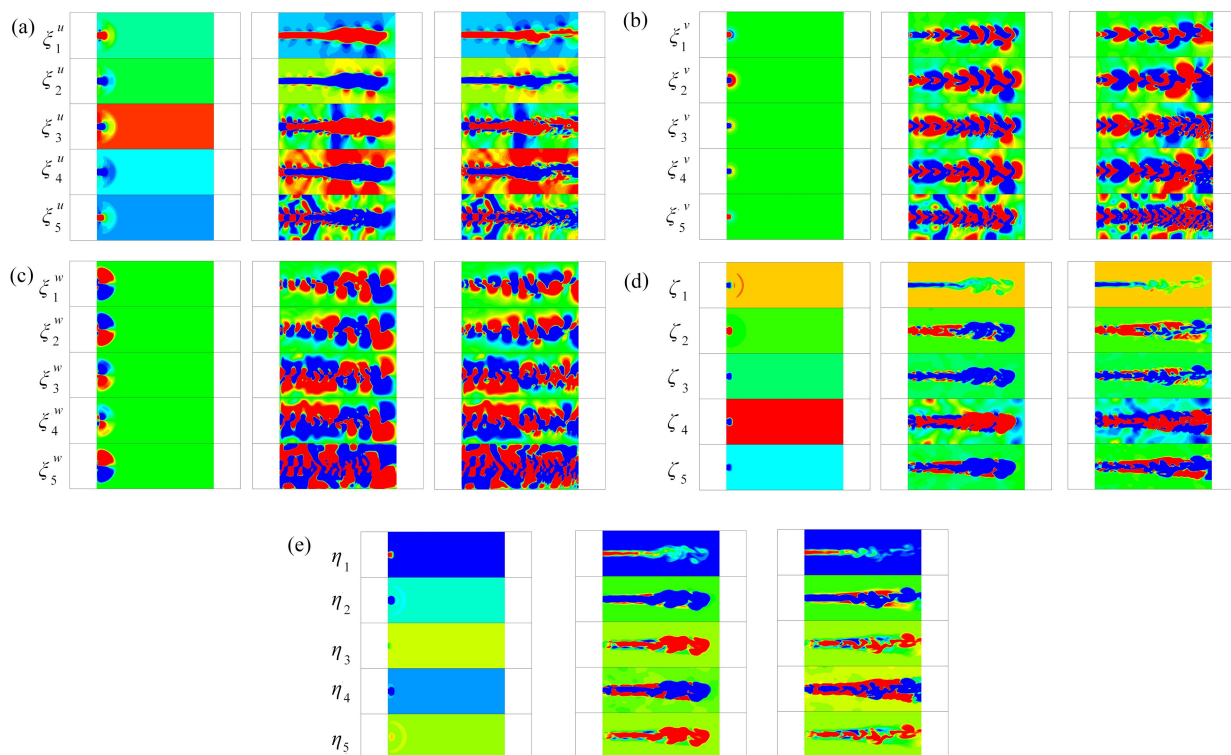


Fig. 18 Time evolution of spatiotemporal-coupling optimal velocity basis ξ , density basis ζ and temperature basis η : from left to right, $t = 100$ s, 3 000 s, 6 000 s

6 Conclusions and the Future Work

6.1 Conclusions

From the above results, one can draw the following conclusions.

First, the concept of traditional spectrum expansion based on the separation of variables and known spatial basis functions is extended to the spatiotemporal-coupling spectrum expansion with the SCOBs satisfying various complex boundary conditions and physical constraints.

Second, the numerical experiment (fig. 4) shows that all low-dimensional dynamical system models based on spatial bases are not predictable.

Third, the accurate quantitative comparison between solutions of the SCOLDDs and the CFD for compressible Navier-Stokes equations shows that, the whole field error is typically below $10^{-2}\%$, and the average error at each cell point is below $10^{-8}\%$, thus ensuring that the approximate solution of the SCOLDDs is in the attraction domain of the numerical solution of the CFD (and the infinite-dimensional Navier-Stokes equations). Then, the accurate dynamical system characteristics of the Navier-Stokes equations can be obtained through analysis of the characteristics of SCOLDDs.

Fourth, the solution of the SCOLDDs for compressible Navier-Stokes equations can be used to approximate the numerical solution of LES equations, which shows through analysis of the characteristics of the SCOLDDs for the Navier-Stokes equations, the accurate turbulent dynamical system characteristics of the LES equation can be obtained.

Finally, using SCOBs is the key to constructing the SCOLDDs. It can obtain the qualitative analysis results of the dynamical system and be quantitatively compared to real flow with very low-dimensional spatiotemporal-coupling intrinsic bases, to ensure the characteristics of SCOLDDs are the dynamic characteristics of the real flow

(such as turbulence).

6.2 The Future Work

The traditional PDE dynamical system models are based on spatial bases, and the objects of dynamical system analysis are limited to the time evolution characteristics of the coefficients of spatial bases, such as bifurcation and chaos. In this study, the modelling theory of SCOLDDS is proposed, and the SCOLDDS model, which is quantitatively comparable to the solution of the infinite-dimensional dynamical system, is obtained, which provides a new research idea and possibility for understanding the characteristics of SCOLDDS for complex flow including compressible turbulence. Therefore, it is necessary to develop a set of corresponding SCOLDDS analysis methods to study the evolution rules and characteristics of complex spatiotemporal-coupling dynamics of real compressible turbulence.

This paper focuses on the modelling theory for OLDDES with spatiotemporal-coupling for compressible flow. The results of the modelling theory of SCOLDDS for incompressible flow will be published elsewhere.

The method of optimal low-dimensional dynamical systems based on spatiotemporal bases is successfully used to the develop a new LES method for compressible turbulent flows, which will published elsewhere.

Acknowledgments The 2nd author extends his appreciation to his former student Mr. WANG Jincheng for his help in this study.

Appendix A The Conjugate Gradient Numerical Optimization Algorithm

The conjugate gradient method^[41] is used to optimize eq. (17). The specific steps of the algorithm are as follow:

1) A set of initial bases $\xi_k^{(0)}$, maximum iteration steps i_{\max} , initial penalty factor $\mu^{(0)}$, optimal bases convergence condition ε_1 and orthogonality convergence condition ε_2 are given.

2) Let $i = 0$.

3) Substitute $\xi_k^{(i)}$ into the equation of a_k and solve $a_k^{(i)}$.

4) Substitute $\xi_k^{(i)}$ and $a_k^{(i)}$ into the generalized optimal objective functional gradient equation to calculate ∇J^g .

5) Let $\mathbf{g}^{(i)}(\mathbf{x}) = \mathbf{h}^{(i)}(\mathbf{x}) = -\nabla J^g$.

6) If $\mathbf{g}^{(i)}(\mathbf{x}) = \mathbf{0}$, proceed to step 11); otherwise, let $\xi_k^{(i+1)} = \xi_k^{(i)}$.

7) Use the 1D search method^[41] to find $\rho^* > 0$, so that

$$J^g(\xi_k^{(i+1)} + \rho^* \mathbf{h}^{(i)}) = \min_{\rho} [J^g(\xi_k^{(i+1)} + \rho \mathbf{h}^{(i)}) | \rho > 0].$$

8) Let $\tilde{\xi}_k = \xi_k^{(i)} + \rho^* \mathbf{h}^{(i)}$.

9) Use $\tilde{\xi}_k$ to perform steps 3) and 4) to obtain $\tilde{a}_k^{(i)}$ and $\tilde{\lambda}_k^{(i)}$, respectively, and perform step 5) to calculate $\nabla \tilde{J}^g$.

10) Uniting $\tilde{\xi}_k$, check whether $\nabla \tilde{J}^g = 0$ and the maximum errors of orthogonality conditions ε_1 and ε_2 are satisfied. If both are satisfied, output the result and stop the calculation. Otherwise, if ε_1 is not satisfied, let

$$\begin{aligned} \mathbf{g}^{(i+1)} &= -\nabla \tilde{J}^g, \\ \mathbf{h}^{(i+1)} &= \mathbf{g}^{(i+1)} + \beta_i \mathbf{g}^{(i)}, \end{aligned}$$

where

$$\beta_i = \frac{(\mathbf{g}^{(i+1)} - \mathbf{g}^{(i)}, \mathbf{g}^{(i+1)})}{\|\mathbf{g}^{(i)}\|^2},$$

and implement step 11). If only ε_2 is not satisfied, let $\mu^{(i+1)} = 10\mu^{(i)}$ and execute step 3).

11) If $i > i_{\max}$, the calculation fails and stops. Otherwise, let $i = i + 1$, $\xi_k^{(i+1)} = \tilde{\xi}_k^{(i)}$, proceed to step 7).

References:

- [1] POPE S B. *Turbulent Flows*[M]. Cambridge: Cambridge University Press, 2000.

- [2] HOFMES P, LUMLEY J L, BERKOOZ G. *Turbulence, Coherent Structures, Dynamical Systems and Symmetry*[M]. Cambridge: Cambridge University Press, 1996.
- [3] HOLMES P, LUMLEY J L, BERKOOZ G, et al. *Turbulence, Coherent Structures, Dynamical Systems and Symmetry*[M]. Cambridge: Cambridge University Press, 2012.
- [4] HALLER G. Lagrangian structures coherent[J]. *Annual Review of Fluid Mechanics*, 2015, **47**: 137-162.
- [5] MENEVEAU C. Lagrangian dynamics and models of the velocity gradient tensor in turbulent flows[J]. *Annual Review of Fluid Mechanics*, 2011, **43**: 219-245.
- [6] REMPFER D. Low-dimensional modeling and numerical simulation of transition in simple shear flows[J]. *Annual Review of Fluid Mechanics*, 2003, **35**: 229-265.
- [7] WIGGINS S. The dynamical systems approach to Lagrangian transport in oceanic flows[J]. *Annual Review of Fluid Mechanics*, 2005, **37**: 295-328.
- [8] SHIRER H N. *Nonlinear Hydrodynamic Modeling: a Mathematical Introduction*[M]. Springer-Verlag, 1987.
- [9] DANIELSON T J, OTTINO J M. Structural stability in two-dimensional model flows: Lagrangian and Eulerian turbulence[J]. *Physics of Fluids A*, 1990, **2**(11): 2024-2035.
- [10] LUMLEY J L. The structure of inhomogeneous turbulent flows[C]//*Atmospheric Turbulence and Radio Wave Propagation*. Moscow: Nauka, 1967: 166-178.
- [11] POJE C, LUMLEY J L. A model for large scale structures in turbulence shear flows[J]. *Journal of Fluid Mechanics*, 1995, **285**: 349-369.
- [12] LUMLEY J L. Coherent structures in turbulence[J]. *Transition and Turbulence*, 1981: 215-242.
- [13] LOÉVE M. *Probability Theory*[M]. Princeton: D. Van Nostrand Co Inc, 1963: 477-485.
- [14] PREISENDORFER R W. *Principal Component Analysis in Meteorology and Oceanography*[M]. Elsevier, 1988.
- [15] BERKOOZ G, HOLMES P, LUMLEY J L. The proper orthogonal decomposition in the analysis of turbulent flows[J]. *Annual Review of Fluid Mechanics*, 1993, **25**: 539-575.
- [16] WU C J. Optimal truncated low-dimensional dynamical systems[J]. *Discrete and Continuous Dynamical Systems*, 1996, **2**(4): 559-583.
- [17] WU C J, SHI H S. An optimal theory for an expansion of flow quantities to capture the flow structures[J]. *Fluid Dynamics Research*, 1996, **17**(2): 67-85.
- [18] WANG L. Applications of optimization methods in fluid mechanics[D]. Master Thesis. Nanjing: PLA University of Science and Technology, 2003.
- [19] WU C J, WANG L. A method of constructing a database-free optimal dynamical system and a global optimal dynamical system[J]. *Science in China, Series G: Physics, Mechanics and Astronomy*, 2008, **51**(7): 905-915.
- [20] WU C J, ZHAO H L. Optimal low dimensional dynamical system modeling method for coherent structure of turbulence[C]//*Proceedings of the Fifth National Conference on Turbulence and Flow Stability*. Wuhan: Chinese Society of Mechanics, 1997.
- [21] WU C J, ZHAO H L. Generalized HWD-POD method and coupling low-dimensional dynamical systems on turbulence, dynamical systems and differential equation[J]. *American Institute of Mathematical Sciences*, 2001, **2001**: 371-379.
- [22] WU C J, ZHAO H L. A new database-free method of constructing optimal low-dimensional dynamical system and its application[J]. *Acta Mechanica Sinica*, 2001, **33**(3): 289-300.
- [23] ZHAO H L. Optimal low-dimensional dynamical systems in fluid dynamics[D]. Master Thesis. Nanjing: Air Force Institute of Meteorology, 1998.
- [24] PENG N F, GUAN H, WU C J. Research on the optimal dynamical systems of three-dimensional Navier-Stokes equations based on weighted residual[J]. *Science China: Physics, Mechanics & Astronomy*, 2016, **59**(4): 644701.
- [25] PENG N F, GUAN H, WU C J. Optimal dynamical systems of Navier-Stokes equations based on generalized helical-wave bases and the fundamental elements of turbulence[J]. *Science China: Physics, Mechanics & Astronomy*, 2016, **59**(11): 114713.
- [26] WANG J C, QI J, WU C J. Analysis and modelling of optimal dynamical systems of incompressible Navier-

- Stokes equations[J]. *Applied Mathematics and Mechanics*, 2020, **41**(1): 1-15.
- [27] WANG J C, QI J, WU C J. Modelling and dynamics analysis of optimal dynamical systems of fluctuation velocity equations for incompressible Navier-Stokes equations[J]. *Applied Mathematics and Mechanics*, 2020, **41**(3): 235-249.
- [28] WANG J C, QI J, WU C J. Modelling and analysis of optimal dynamical systems of incompressible Navier-Stokes equations with pressure base functions[J]. *Applied Mathematics and Mechanics*, 2020, **41**(8): 817-833.
- [29] LEONI G. A first course in Sobolev spaces[D]. Pittsburgh: Carnegie Mellon University, 2009.
- [30] ZHANG G Q, LIN Y Q. *Lecture Notes of Functional Analysis*[M]. Beijing: Peking University Press, 2013.
- [31] HAND L N, FINCH J D. *Analytical Mechanics*[M]. Cambridge: Cambridge University Press, 1998.
- [32] SAMTANEY R, PULLIN D I, KOSOVIĆ B. Direct numerical simulation of decaying compressible turbulence and shocklet statistics[J]. *Physics of Fluids*, 2001, **13**(5): 1415-1430.
- [33] SHEN W D, TONG J G. *Engineering Thermodynamics*[M]. Beijing: Higher Education Press, 2007: 62-63.
- [34] ZHANG Y J, WANG P, HAN Z X, et al. *Complete Works of Fluid Mechanics*[M]. Beijing: Beijing University of Aeronautics and Astronautics Press, 1991.
- [35] SUTHERLAND W. The viscosity of gases and molecular force[J]. *Philosophical Magazine*, 1893, **36**(223): 507-531.
- [36] FORD W. *Numerical Linear Algebra With Applications*[M]. London: Academic Press, 2014.
- [37] BUI T T. A parallel, finite-volume algorithm for large-eddy simulation of turbulent flows[J]. *Computers & Fluids*, 2000, **29**(8): 877-915.
- [38] FAVRE A. Equations des gazturbulents compressible, I : forms generals[J]. *Journal de Mécanique*, 1965, **4**(2): 361.
- [39] FAVRE A. Equations des gazturbulents compressible, II : méthode des vitesses moyennes, méthode des vitesses macroscopiques pondérées par la mass volumique[J]. *Journal de Mécanique*, 1965, **4**(3): 391.
- [40] SMAGORINSKY U. General circulation experiments with the primitive equations, I : the basic experiment[J]. *Monthly Weather Review*, 1963, **91**(3): 99-164.
- [41] YE Q K, WANG Z M. *Numerical Methods in Optimization and Optimal Control*[M]. Beijing: Science Press, 1986.